# Atmospheric oxidation capacity and ozone pollution mechanism in a coastal city of Southeast China: Analysis of a typical photochemical episode by Observation-Based Model

Taotao Liu[1,2,3], Youwei Hong[1,2], Mengren Li[1,2], Lingling Xu[1,2], Jinsheng Chen[1,2]*, Yahui Bian[1,2], Chen Yang[1,2,3], Yangbin Dan[1,2], Yingnan Zhang[4], Likun Xue[4]*, Min Zhao[4], Zhi Huang[5], Hong Wang[6]

[1]Center for Excellence in Regional Atmospheric Environment, Institute of Urban Environment, Chinese Academy of Sciences, Xiamen, China
[2]Key Lab of Urban Environment and Health, Institute of Urban Environment, Chinese Academy of Sciences, Xiamen, China
[3]University of Chinese Academy of Sciences, Beijing, China
[4]Environment Research Institute, Shandong University, Jinan, Shandong, China
[5]Xiamen Institute of Environmental Science, Xiamen, China
[6]Fujian Meteorological Science Institute, Fujian Key Laboratory of Severe Weather, Fuzhou, China

Corresponding authors E-mail: Jinsheng Chen (jschen@iue.ac.cn); Likun Xue (xuelikun@sdu.edu.cn)

**Abstract:**

A typical multi-day ozone ($O_3$) pollution event was chosen to explore the atmospheric oxidation capacity (AOC), OH reactivity, radical chemistry, and $O_3$ pollution mechanism in a coastal city of Southeast China, with an Observation-Based Model coupled to the Master Chemical Mechanism (OBM-MCM). The hydroxyl radical (OH) was the predominant oxidant (90±25%) for daytime AOC, while $NO_3$ radical played an important role for AOC during the nighttime (72±9%). Oxygenated volatile organic compounds (OVOCs, 30±8%), $NO_2$ (29±8%) and CO (25±5%) were the dominant contributors to OH reactivity, accelerating the production of $O_3$ and recycling of ROx radicals (ROx=OH+$HO_2$+$RO_2$). Photolysis of nitrous acid (HONO, 33±14%), $O_3$ (25±13%), formaldehyde (HCHO, 20±5%), and other OVOCs (17±2%) were major ROx sources, which played initiation roles in atmospheric oxidation processes. ~~$O_3$ formation was VOC-sensitive, and controlling emissions of aromatics, alkenes, and long-chain alkanes were benefit for ozone pollution mitigation.~~ Combined with regional transport analysis, the reasons for this $O_3$ episode were the accumulation of local photochemical production and regional transport. The results of sensitivity analysis showed that VOCs were the limiting factor of radical recycling and $O_3$ formation, and the 5% reduction of $O_3$ would be achieved by decreasing 20% anthropogenic VOCs, and controlling emissions of aromatics, alkenes, and alkanes with ≥4 carbons were benefit for ozone pollution mitigation. The findings of this study have significant guidance for emission reduction and regional collaboration on future photochemical pollution control in the relatively clean coastal cities of China and similar countries.

**Keywords**: Atmospheric oxidation capacity; Radical chemistry; $O_3$ formation mechanism; OH reactivity; OBM-MCM

## 1 Introduction

Tropospheric ozone ($O_3$) is mainly produced by photochemical reactions of anthropogenic and natural emitted volatile organic compounds (VOCs) and nitrogen oxides (NOx), and is an important factor resulting in regional air pollution (Zhu et al., 2020; Lu et al., 2018). The elevated $O_3$ concentrations enhance the atmospheric oxidation capacity (AOC) and have harmful effects on global climate change, ecosystems, and human health (Liu et al., 2019a; Fowler et al., 2009). The formation mechanisms of $O_3$ pollution are extremely difficult to figure out, due to the complex types and sources of its precursors (Simon et al., 2015). $O_3$ formation is affected by multiple factors such as ~~temporal & spatial distribution~~$O_3$ precursor speciation or level, atmospheric oxidation capacity, meteorological conditions and regional transport (Gong and Liao, 2019; Chang et al., 2019). To effectively control the tropospheric $O_3$ pollution, exploration of the photochemical mechanism and judgment on the controlling factors of $O_3$ formation become extremely important for scientific community (Chen et al., 2020; Li et al., 2018).

The atmospheric oxidation capacity reflects the essential driving force in tropospheric chemistry, and plays an important place in the ~~destruction~~ loss rates of primary components and production rates of secondary pollutants ~~(Elshorbany et al., 2008).~~, thus the key factors to quantify AOC are processes and rates of species being oxidized in the atmosphere (Elshorbany et al., 2009). The atmospheric conditions (such as photolysis rate, meteorology, pollutant concentrations and regional transport) together influence the AOC levels, and the AOC levels in the polluted urban regions are generally much higher than those at the background sites or remote regions due to the dominant limited factor for the significant differences of pollutant concentrations ~~(~~Geyer et al., 2001; Xue et al., 2016). ROx radicals, including hydroxyl radical (OH), hydro peroxy radical ($HO_2$) and organic peroxy radical ($RO_2$), are very important indicators in atmospheric photochemistry and dominate the atmospheric ~~oxidative~~ oxidation capacity (Li et al., 2018). Meanwhile, radical chemistry drives the transformation and recycling of $O_3$ through initiating atmospheric oxidation processes (Wang et al., 2020). Among these radicals, the OH radical accounts for the majority of AOC over 90% during the daytime, thus the OH reactivity (i.e., OH loss) indicates the primary contribution of individual pollutants (Wang et al., 2018a; Mao et al., 2010). Hence, atmospheric oxidation capacity, OH reactivity, and radical chemistry are crucial aspects for understanding the complex atmospheric photochemistry processes (Li et al., 2018). For example, the major ~~primary~~ ROx sources are

the photolysis reaction of $O_3$, formaldehyde (HCHO), other oxygenated volatile organic compounds (OVOCs), nitrous acid (HONO) and the reactions of $O_3$ with unsaturated VOCs (Volkamer et al., 2010). The dominant ROx sources at some rural sites were $O_3$ photolysis and $O_3$ reactions with VOCs (Li et al., 2018; Martinez et al., 2003), and those at many urban sites were HONO and OVOCs photolysis (Xue et al., 2016; Liu et al., 2012; Emmerson et al., 2005). For oil and gas field sites, there were highly abundant VOCs to promote the formations of $O_3$, and the contribution of OVOCs photolysis was 2-5 times higher than that in urban areas (Chen et al., 2020; Edwards et al., 2013, 2014). The HONO photolysis was a very important ~~primary~~ ROx source at the high-altitude or background sites. (Acker et al., 2001; Jiang et al., 2020).

Current studies of atmospheric $O_3$ photochemical pollution observations have been conducted at the urban, suburban, rural and remote sites around the world (Smith et al., 2006; Eisele et al., 1997; Kanaya et al., 2001; Hofzumahaus et al., 2009; George et al., 1999; Emmerson et al., 2005; Kanaya et al., 2007; Michoud et al., 2012). In China, $O_3$ photochemical pollution events have been reported in some megacities, such as Beijing, Shanghai, Guangzhou, and Chengdu (Liu et al., 2012; Tan et al., 2019; Zhu et al., 2020; Wang et al., 2020; Liu et al., 2019b; Ling et al., 2017). Few studies on $O_3$ photochemical pollution in cities with low $O_3$ precursor emissions have been reported, and the air quality in these areas usually depends on the change of meteorological conditions. In a coastal city of Southeast China, the concentrations of $O_3$ precursors were higher than those in remote sites and background, but lower than those in most urban and suburban areas, even lower than those in rural regions (Table S1). In a word, $O_3$ precursor emissions in our observation site were relatively low. Meanwhile, the southeast coastal region is influenced by the East Asian monsoon and acts as an important transport path between the Yangtze River Delta (YRD) and the Pearl River Delta (PRD) (Liu et al., 2020a; Liu et al., 2020b), which is a good 'laboratory' to further explore $O_3$ photochemical pollution and formation mechanism with relatively low $O_3$ precursors and complex meteorological conditions (Zhang et al., 2020b; Hu et al., 2020).

The Observation-Based Model (OBM) is widely used to investigate $O_3$-VOCs-NOx relationships and radical chemistry (Wang et al., 2018a; Tan et al., 2019). The $O_3$ sensitivity ~~reveals~~ revealed the non-linear relationship between $O_3$ and its precursors (i.e., VOCs and NOx), which was conducted to investigate $O_3$ formation mechanism and control strategies (Wang et al., 2020). The OBM combined with the Master Chemical Mechanism (V3.3.1) (OBM-MCM) has been applied to explore the $O_3$ photochemical pollution mechanism in different environmental conditions (Chen et al., 2020; Li et al., 2018; Xue et al., 2016; Wang et al., 2018). In this study, we chose a typical multi-day $O_3$ pollution event in the coastal city Xiamen (Fig. S1), when Xiamen was affected by various meteorological conditions, such as typhoon and the West Pacific Subtropical High (WPSH) accompanied by temperature inversion

phenomenon. Based on the OBM-MCM analyses, the study aims to clarify (1) the pollution characteristics of $O_3$ and its precursors, (2) the atmospheric oxidation capacity and radical chemistry, and (3) the $O_3$ formation mechanism and sensitivity analysis. The results are expected to enhance the understanding of the $O_3$ formation mechanism with low $O_3$ precursor levels, and provide scientific evidence for $O_3$ pollution control in the coastal cities.

## 2 Materials and methods

### 2.1 Study area and field observations

Xiamen is a coastal city in the southeast area of China, to the west coast of the Taiwan Strait. The field campaigns were carried out at the Atmospheric Environment Observation Supersite (24.61° N, 118.06° E) on the rooftop of around 70 m high building in the Institute of Urban Environment, Chinese Academy of Sciences. The supersite was equipped with complete monitoring instruments, including gas and aerosol species compositions, $O_3$ precursors, meteorological parameters, and photolysis rate. Criteria air pollutants of $O_3$, $SO_2$, NO-$NO_2$-NOx, and CO were monitored by commercial instruments TEI 49i, 43i, 42i, and 48i (*Thermo Fisher Scientific, USA*), respectively. The meteorological parameters of wind speed (WS), wind direction (WD), air temperature (T), pressure (P), and relative humidity (RH) were measured by an ultrasonic atmospherium (*150WX, Airmar, USA*). HONO was measured with an analyzer for Monitoring Aerosols and Gases in Ambient Air (*MARGA, ADI 2080, Applikon Analytical B.V., the Netherlands*). A gas chromatography-mass spectrometer (GC-FID/MS, *TH-300B, Wuhan, CN*) was used for atmospheric VOCs concentrations monitoring, involving about 103 species of VOCs with a 1-hour time resolution. Photolysis frequencies were measured by a photolysis spectrometer (*PFS-100, Focused Photonics Inc., Hangzhou, China*). The photolysis rate constants include $J(O^1D)$, $J(NO_2)$, $J(H_2O_2)$, $J$(HONO), $J$(HCHO), and $J(NO_3)$. Strict quality assurance and quality control were applied, and the detailed descriptions of the monitoring procedures were documented in our previous studies (Zhang et al., 2020b; Wu et al., 2020; Liu et al., 2020a; Liu et al., 2020b; Hu et al., 2020a).

### 2.2 Observation-based chemical box model

In this study, the Observation-Based Model (OBM) combined with the latest version 3.3.1 of MCM (MCM v3.3.1; http://mcm.leeds.ac.uk/MCM/), involving 142 non-methane VOCs and more than 17000 elementary reactions of 6700 primary, secondary and radical species (Jenkin et al., 2003; Saunders et al., 2003), was used to explore the atmospheric oxidation processes and $O_3$ formation mechanisms. The physical process of deposition within the boundary layer height (BLH), which varied from 300 m during

nighttime to 1500 m during the daytime in autumn (Li et al., 2018), was considered in the model. Therefore, the dry deposition velocity was utilized to simulate the deposition loss of some reactants in the atmosphere and showed in Table S2, which avoided continuous accumulation of pollutant concentrations in the model (Zhang et al., 2003; Xue et al., 2016).

The observation ~~data~~ parameters of the gaseous pollutants (i.e., $O_3$, CO, NO, $NO_2$, HONO, $SO_2$, and VOCs), meteorological parameters (i.e., T, P, and RH), and photolysis rate constants ($J(O^1D)$, $J(NO_2)$, $J(H_2O_2)$, $J$(HONO), $J$(HCHO), and $J(NO_3)$) were input into the OBM-MCM model as constraints. The photolysis rates of other molecules such as OVOCs were parameterized by solar zenith angle and then scaled by the measured $J(NO_2)$ (Saunders et al., 2003). We pre-ran for 5 days before running the model to initialize the unmeasured compounds and radicals (Xue et al., 2014).

OBM-MCM is mainly used to simulate in situ atmospheric photochemical processes and quantify the $O_3$ production rate, AOC, OH reactivity, and ROx radical budgets. Among them, primary sources of ROx, including the photolysis reactions of $O_3$, HONO, formaldehyde (HCHO), and other OVOCs as well as reactions of VOCs with $O_3$ and $NO_3$ radicals, are important (Xue et al., 2016). The termination reactions of ROx are controlled by cross-reactions with NOx (under high NOx conditions) and ROx (under low NOx conditions) to form nitric acid, organic nitrates, and peroxides (Liu et al., 2012; Xue et al., 2016). Table 1 shows the production and destruction reactions and relevant reaction rates of $O_3$ in our study. The production rate of $O_3$ ($P(O_3)$) includes $RO_2$+NO (R1) and $HO_2$+NO reactions (R2, Eq. 1), and the destruction of $O_3$ ($D(O_3)$) involves reactions of $O_3$ photolysis (R3), $O_3$+OH (R4), $O_3$+$HO_2$ (R5), $NO_2$+OH (R6), $O_3$+VOCs (R7), and $NO_3$+VOCs (R8, Eq. 2). The net $O_3$ production rate ($Pnet(O_3)$) is calculated by $P(O_3)$ minus $D(O_3)$ as equation 3.

**Table 1 Simulated production and destruction reactions and relevant reaction rates of $O_3$ in our study.**

| Reactions | Reaction rates | Number |
|---|---|---|
| **$O_3$ production pathways-P($O_3$)** | | |
| $RO_2$+NO→RO+$NO_2$ | $2.7\times10^{-12}\times EXP(360/T)$ | R1 |
| $HO_2$ +NO→OH+$NO_2$ | $3.45\times10^{-12}\times EXP(270/T)$ | R2 |
| **$O_3$ loss pathways-D($O_3$)** | | |
| $O_3$+hv→$O^1D$+$O_2$ | $JO^1D$ | R3a |
| $O^1D$+$H_2O$→OH | $2.14\times10^{-10}$ | R3b |
| $O_3$+OH→$HO_2$ | $1.70\times10^{-12}\times EXP(-940/T)$ | R4 |
| $O_3$+$HO_2$→OH | $2.03\times10^{-16}\times(T/300)^{4.57}\times EXP(693/T)$ | R5 |
| $NO_2$+OH→$HNO_3$ | $3.2\times10^{-30}\times9.7\times10^{18}\times P/T\times(T/300)^{-4.5}\times3.0^{-11}\times10^{\log_{10}(0.41)}/(1+(\log(3.2^{-30}\times9.7E\times10^{18}\times P/T\times(T/300)^{-4.5}\times3.0^{-11}/(0.75-1.27\times(\log_{10}(0.14))^2)/(3.2^{-30}\times9.7E\times10^{18}\times P/T\times(T/300)^{-4.5}+3.0^{-11})$ | R6 |
| $O_3$+VOCs→Carbonyls+Criegee biradical | Kcons.1 | R7 |

| | | |
|---|---|---|
| $NO_3$+VOCs→$RO_2$ | Kcons.2 | R8 |

Note: The reaction rates of Kcons.1 and Kcons.2 were constant. There were around 700 reactions of VOCs+$NO_3$/$O_3$, and the relevant reaction rates were different, which can be obtained from this website http://mcm.leeds.ac.uk/MCM/.

$$P(O_3) = k_1[HO_2][NO] + \sum(k_{2i}[RO_2][NO]) \quad (1)$$

$$D(O_3) = k_3[O_1D][H_2O] + k_4[O_3][OH] + k_5[O_3][HO_2] + k_6[NO_2][OH] + \sum(k_{7i}[O_3][unsat.VOCs]) + 2\sum(k_{8i}[NO_3][unsat.VOCs]) \quad (2)$$

$$Pnet(O_3) = P(O_3) - D(O_3) \quad (3)$$

where *ki* is the related reaction rate constant. Detailed descriptions of the chemistry calculation can be found elsewhere (Chen et al., 2020; Wang et al., 2018a; Xue et al., 2014).

Relative incremental reactivity (RIR), an index to diagnose the sensitivity of $O_3$ formation to precursors, is defined as the ratio of the differences in $O_3$ production rate to the difference in precursor concentrations (Chen et al., 2020). Here, the $\Delta X/X$ in the OBM-MCM represents the percentage reduction in the input concentrations of each targeted $O_3$ precursor group and this value is adopted as 20% (Liu et al., 2020c).

$$RIR = \frac{\Delta P(O_3)/P(O_3)}{\Delta X/X} \quad (4)$$

## 2.3 Model performance

The index of agreement (IOA) can be used to judge the reliability of the model simulation results, and its equation is (Liu et al., 2019b):

$$IOA = 1 - \frac{\sum_{i=1}^{n}(O_i - S_i)^2}{\sum_{i=1}^{n}(|O_i - \bar{O}| - |S_i - \bar{O}|)^2} \quad (5)$$

where *Si* is simulated value, *Oi* represent observed value, $\bar{O}$ the average observed values, and n is the sample number. The IOA range is 0-1, and the higher the IOA value is, the better agreement between simulated and observed values is. In many studies, when IOA ranges from 0.68 to 0.89 (Wang et al., 2018b), the simulation results are reasonable, and the IOA in our research is 0.80. Hence, the performance of the OBM-MCM model was reasonably acceptable.

## 2.43 Meteorological data and back trajectory calculation

The backward trajectories of air masses arriving at the observation site were calculated by the MeteoInfo during the episode (Wang *et al*., 2014). The backward trajectories with 72-h were run with the time resolution of 3 hours at 100 m height above ground level, and starting time was 0:00 LT and the

ending time was 23:00 LT. Meteorological data were provided by NOAA ARL (ftp://arlftp.arlhq.noaa.gov/pub/archives/gdas1). The Final Operational Global Analysis data (FNL) is from the Global Data Assimilation System and analyzes results with the model which is also used by the National Center for Environmental Prediction (NCEP) in the Global Forecast System (GFS) (https://rda.ucar.edu/datasets/ds083.2/). The weather charts were conducted using Grid Analysis and Display System (GrADS) with the specific programmed script files. A detailed description of the synoptic information was shown in our previous study (Wu et al., 2019).

## 3 Results and discussion

### 3.1 Overview of observations

The $O_3$ pollution events frequently appeared in the coastal city Xiamen during autumn time, related to the ~~West Pacific Subtropical High (~~WPSH~~)~~, carrying favorable photochemical reaction conditions (high temperature, low RH, and stagnant weather conditions~~,~~ ) and encouraging the formation and accumulation of $O_3$ in the southeast coastal area (Wang et al., 2018a). The daily maximum 8-h-average $O_3$ concentrations (MDA8h $O_3$) from 20 to 29 Sep~~,~~ 2019 ranged from 53 to 85 ppbv, partly exceeding the Grade II of China's National Ambient Air Quality Standard of 75 ppbv. The time series and descriptive statistics of air pollutants and meteorological parameters during this multi-day $O_3$ pollution event are shown in Fig. 1 and Table ~~1~~2. During this period, the dominant wind direction was northeast, with an average wind speed of 1.8±0.9 $m \cdot s^{-1}$. The maximum hourly temperature was as high as 35 ℃, and the average RH was 56.4±12.6%. Our previous study showed that particulate pollution was slight in Xiamen, which could affect solar radiation by light-absorbing component, and the concentrations of particulate matter had not exceeded the National Ambient Air Quality Standard (Class II: 75 $\mu g \cdot m^{-3}$) for a whole year (Hu et al., 2021; Deng et al., 2020). Therefore, solar radiation intensity and J($NO_2$) were strong, compared to those of the Yellow River Delta (Chen et al., 2020), Shanghai (Zhu et al., 2020) and Hong Kong (Xue et al., 2016). In general, these meteorological parameters were conducive to the production and accumulation of $O_3$. In addition, $O_3$ concentrations at nighttime kept relatively high (Fig.1), indicating the influence of regional transport and little NO titration (Zhang et al., 2020a; Wu et al., 2020). Figure S2 shows the 72 h back trajectories at the monitoring site. Among them, 80% of the air masses came from the Yellow Sea, and the other 20% air masses originated from the northeast China through long-range transport.

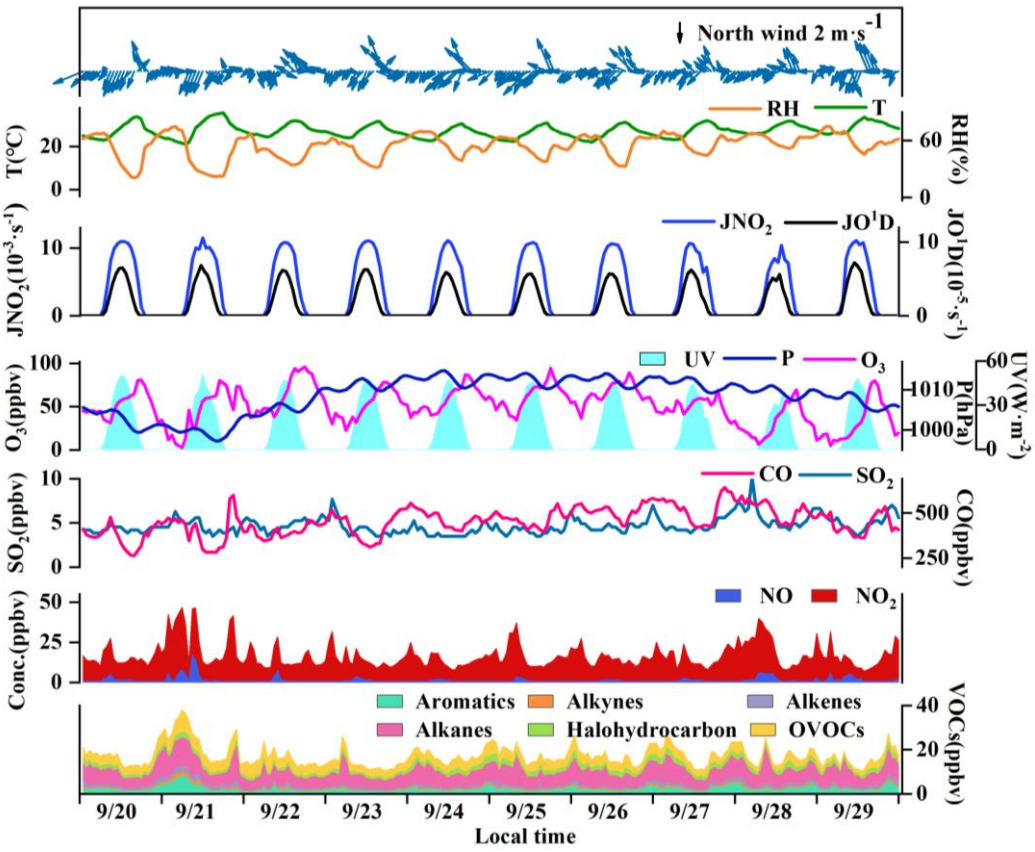


**Figure 1. Time series of major trace gases, photolysis rate constants, and meteorological parameters during 20-29 Sep. 2019 in Xiamen.**

**Table ~~1~~2. Descriptive statistics of major trace gases (ppbv) and meteorological parameters during 20-29 Sep. 2019**

| Parameters | Mean±SD | Median | Max |
|---|---|---|---|
| MDA8h $O_3$ | 67.4±17.2 | 52.6 | 89.3 |
| TVOCs | 17.2±4.8 | 16.1 | 38.0 |
| CO | 452±77.3 | 454 | 641 |
| NO | 1.4±1.3 | 0.8 | 17.1 |
| $NO_2$ | 15.4±6.9 | 13.6 | 40.9 |
| $SO_2$ | 4.7±0.9 | 4.6 | 10.2 |
| T (℃) | 27.3±3.21 | 26.9 | 35.6 |
| RH (%) | 56.4±12.6 | 56.6 | 75.0 |
| P (hPa) | 1008±4.57 | 1010 | 1015 |
| UV ($W·m^{-2}$) | 46.4±1.12 | 0 | 51.1 |
| Wind speed ($m·s^{-1}$) | 1.8±0.9 | 1.6 | 3.8 |
| Wind direction (◦) | 90.8±90.4 | 45.0 | 337 |

**Table ~~2~~3. Measured VOCs concentrations during 20-29 Sep. 2019 in Xiamen (Units: pptv), and the classification of VOCs were used and introduced in Section 3.3.**

| Chemicals | Classification | Mean±SD | Chemicals | Classification | Mean±SD |
|---|---|---|---|---|---|
| **Aromatics** | | **2131±1236** | **Alkanes** | | **6970±2325** |
| toluene | RAROM/AHC | 995±632 | ethane | LRHC/AHC | 1552±342 |
| m/p-xylene | RAROM/AHC | 392±326 | propane | LRHC/AHC | 1546±608 |
| benzene | LRHC/AHC | 236±95 | iso-pentane | C4HC/AHC | 930±316 |
| o-xylene | RAROM/AHC | 154±121 | n-butane | C4HC/AHC | 844±365 |
| ethylbenzene | RAROM/AHC | 138±94 | n-dodecane | C4HC/AHC | 618±101 |
| styrene | RAROM/AHC | 76±65 | iso-butane | C4HC/AHC | 494±201 |
| 1,2,4-trimethylbenzene | RAROM/AHC | 75±37 | n-pentane | C4HC/AHC | 254±157 |

| | | | | | |
|---|---|---|---|---|---|
| m-ethyltoluene | RAROM/AHC | 16±11 | n-hexane | C4HC/AHC | 134±184 |
| p-ethyltoluene | RAROM/AHC | 10±6 | 3-methylhexane | C4HC/AHC | 116±93 |
| iso-propylbenzene | RAROM/AHC | 5±3 | n-heptane | C4HC/AHC | 104±78 |
| 1,3,5-trimethylbenzene | RAROM/AHC | 8±6 | 3-methylpentane | C4HC/AHC | 82±48 |
| o-ethyltoluene | RAROM/AHC | 8±5 | 2-methylhexane | C4HC/AHC | 67±38 |
| 1,2,3-trimethylbenzene | RAROM/AHC | 7±5 | 2-methylpentane | C4HC/AHC | 56±46 |
| n-propylbenzene | RAROM/AHC | 7±4 | 2,3-dimethylbutane | C4HC/AHC | 54±33 |
| **Halocarbons** | | **1951±572** | cyclohexane | C4HC/AHC | 42±15 |
| dichloromethane | AHC | 998±392 | n-undecane | C4HC/AHC | 33±35 |
| 1,2-dichloroethane | AHC | 499±210 | n-octane | C4HC/AHC | 24±15 |
| chloromethane | AHC | 294±75 | n-nonane | C4HC/AHC | 15±13 |
| 1,2-dichloropropane | AHC | 88±34 | 2,2-dimethylbutane | C4HC/AHC | 15±7 |
| bromomethane | AHC | 47±23 | n-decane | C4HC/AHC | 14±11 |
| trichloroethene | AHC | 15±6 | **Alkenes** | | **1205±464** |
| 1,4-dichlorobenzene | AHC | 9±3 | ethene | Alkenes/AHC | 671±361 |
| **OVOCs** | AHC | **4246±1263** | propene | Alkenes/AHC | 207±116 |
| acetone | AHC | 2802±750 | isoprene | BHC | 171±232 |
| 2-butanone | AHC | 799±430 | trans-2-pentene | Alkenes/AHC | 105±62 |
| 2-propanol | AHC | 343±283 | 1-butene | Alkenes/AHC | 16±21 |
| 2-methoxy-2-methylpropane | AHC | 169±97 | cis-2-butene | Alkenes/AHC | 12±12 |
| acrolein | AHC | 66±22 | 1-pentene | Alkenes/AHC | 10±7 |
| 4-methyl-2-pentanone | AHC | 16±15 | 1,3-butadiene | Alkenes/AHC | 8±7 |
| 2-hexanone | AHC | 12±3 | trans-2-butene | Alkenes/AHC | 4±4 |
| | | | **Acetylene** | LRHC/AHC | **674±290** |

Table ~~2~~ 3 lists the detailed VOCs concentrations during the observation period. Alkanes (6970±2325 pptv) were the predominant components of total VOCs, followed by OVOCs (4246±1263 pptv), aromatics (2131±1236 pptv), halocarbons (1951±572 pptv), alkenes (1205±464 pptv), and acetylene (674±290 pptv). The ratio of ethene/ethane (0.4±0.2) was significantly ($p<0.05$) lower than that in Hong Kong (0.7±0.1) with significant aged air masses, indicating that the high $O_3$ in Xiamen might be partially attributed to the aged air masses (e.g., transport of air from polluted regions or intense atmospheric oxidation) (Wang et al., 2018a). The concentration of TVOCs in Xiamen (17.2±4.8 ppbv) was much lower than that in the developed areas with large anthropogenic emissions (i.e., Beijing (44.2 ppbv), Lanzhou (45.3 ppbv), Wuhan (30.2 ppbv), Chengdu (36.0 ppbv), Hong Kong (26.9 ppbv), Los Angeles (41.3 ppbv) and Tokyo (43.4 ppbv), but was higher than that at the background and remote sites (i.e., Mt. Wuyi 4.7 ppbv and Mt. Waliguan 2.6 ppbv) (Table S1).

The $O_3$ formation process depends on its precursors and related environmental conditions, while the photochemical reactions during the daytime are the basis for $O_3$ changes. Figure 2 shows the diurnal patterns of major trace gases and meteorological parameters during 20-29 Sep. 2019. The $O_3$ concentration was maintained at relatively low levels from night to 07:00 LT, then rose and reached its maximum at around 17:00 LT. $O_3$ peak in the afternoon was related to the accumulation of both local

photochemical reaction and potential regional transport (including $O_3$ and its precursors in the upwind direction to the observation site), and the detailed analysis will be shown in Section 3.3.2. The reduction of observed $O_3$ ($\Delta O_3$) in the early morning rush hour caused by NO titration did not appear, verifying the impacts of regional transport (Liu et al., 2019b; Zeren et al., 2019; Chen et al., 2020). Due to the photochemical reactions, the precursors of CO, NOx and VOCs were consumed during the daytime, and were accumulated during the nighttime with weak solar radiation. The diurnal patterns of VOCs ~~and,~~ NOx and CO were similar, with the highest concentrations at around 08:00 LT and then decreasing during 9:00~16:00 LT and increasing at night, which is related to the human activity emissions (especially vehicle exhaust) and the variations of boundary layer (Elshorbany et al., 2009; Hu et al., 2020).

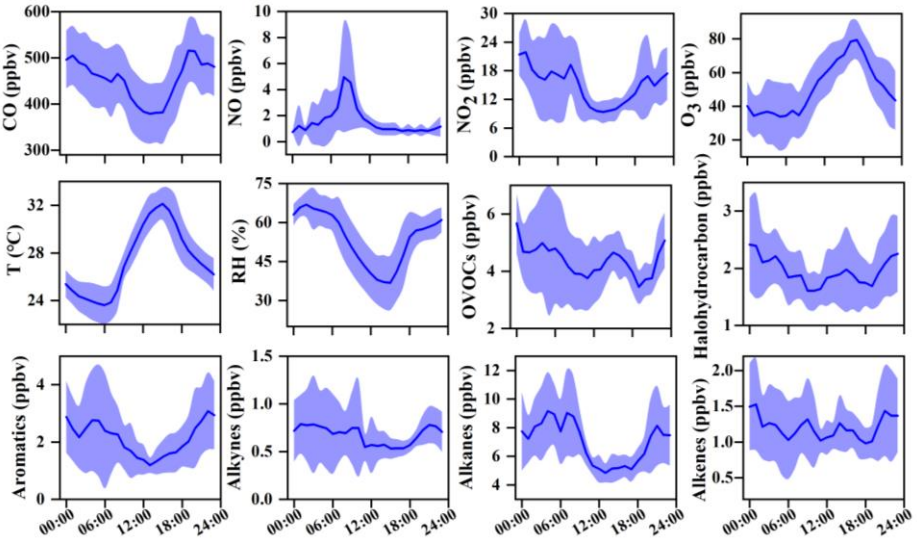


**Figure 2. Average diurnal patterns of major trace gases and meteorological parameters during 20-29 Sep. 2019 in Xiamen. The error bar is the standard error.**

## 3.2 Atmospheric oxidation and radical chemistry

### 3.2.1 Atmospheric oxidation capacity (AOC)

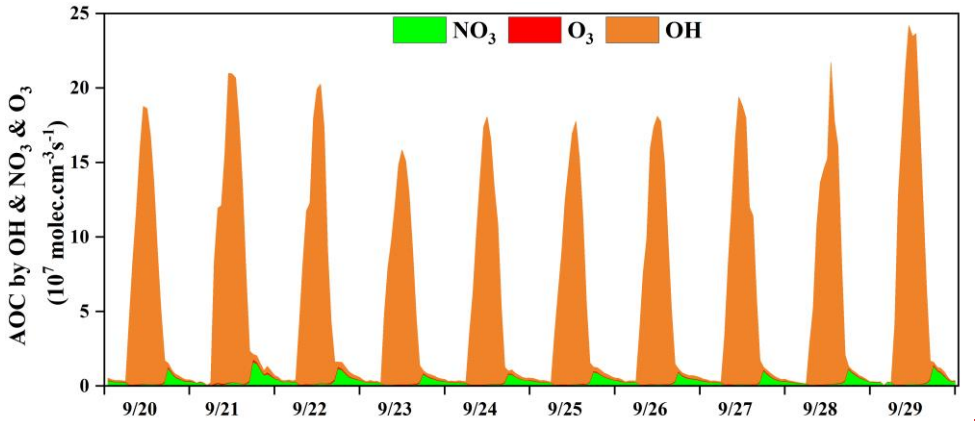

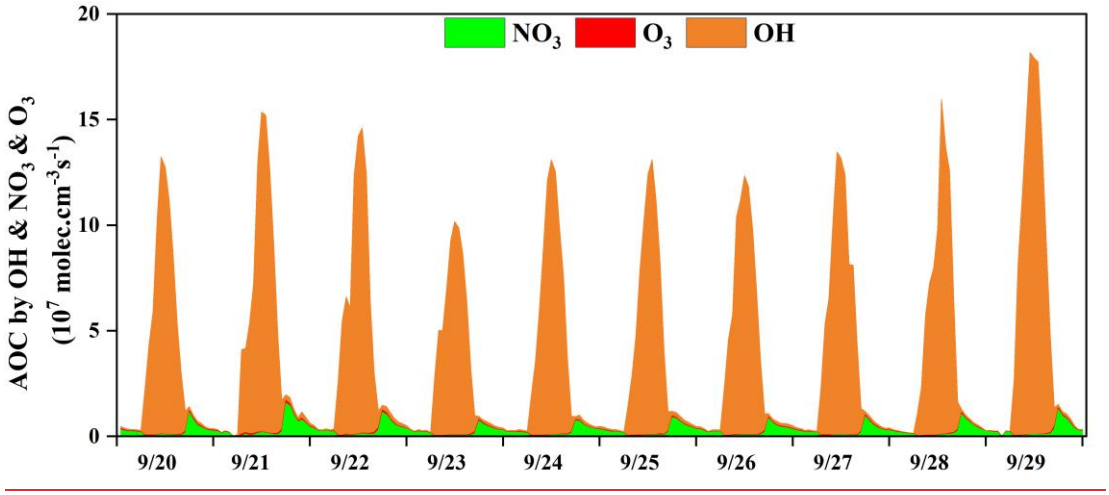


**Figure 3. Time series of the model-calculated Atmospheric Oxidation Capacity (AOC) in Xiamen during 20-29 Sep. 2019.**

Figure 3 shows the time series of the model-calculated AOC during the $O_3$ pollution period. The AOC determines the removal rate of primary pollutants and the production rate of secondary pollutants, and was the basis for reflecting atmospheric photochemical pollution (Geyer et al., 2001). AOC is calculated as the sum of oxidation rates of various primary pollutants (CO, NOx, VOCs, etc.) by the major oxidants (i.e., OH, $O_3$, $NO_3$) (Chen et al., 2020; Xue et al., 2016; Xue et al., 2014). In this study, the average daytime AOC was $6.7\times10^7$ molecules $cm^{-3}$ $s^{-1}$, and the daily maximum AOC was $1.3\times10^8$ molecules $cm^{-3}$ $s^{-1}$, which was higher than those at rural sites with much low pollution emissions in Berlin ($1.4\times 10^7$ molecules $cm^{-3}$ $s^{-1}$) and a regional background in Hong Kong ($6.2 \times 10^7$), but lower than that in polluted cities, such as Santiago ($3.2\times10^8$ molecules $cm^{-3}$ $s^{-1}$), due to the main limited factor of the significant differences of pollutant concentrations among different sites (Li et al., 2018; Xue et al., 2016; Geyer et al., 2001; Zhu et al., 2020). In some urban regions, the concentrations of air pollutants were higher than those in Xiamen, but their AOC levels (Hong Kong: $1.3\times10^8$ molecules $cm^{-3}$ $s^{-1}$; Shanghai: $1.0\times10^8$ molecules $cm^{-3}$ $s^{-1}$) were comparable to or even lower compared with the AOC in Xiamen, which could be attributed to the relatively high solar radiation (Xue et al., 2016; Zhu et al., 2020) (Detailed descriptions showed in Section 3.1). The results of AOC characteristics in different regions were decided by the precursor concentrations/types and photochemical environment.

According to the diurnal patterns of the AOC contributed by OH, $O_3$, and $NO_3$, the predominant oxidant was OH (90±25%) during the daytime, followed by $NO_3$ (8±22%) and $O_3$ (2±3%). Meanwhile, the diurnal characteristics of AOC were consistent with the profile of the model-calculated OH (Fig. ~~S4~~S3) and the observed photolysis rate constants (Fig.1) (Zhu et al., 2020). Meanwhile, $NO_3$ (72±9%) played

the most important role in the oxidant capability during the nighttime, followed by OH (20±12%) and $O_3$ (8±1%). In particular, the contribution of $NO_3$ to AOC reached the maximum of 80% at around 18:00 LT, when the concentrations of $O_3$ and $NO_2$ were relatively high and accelerated the formation of $NO_3$ (Fig.2). In addition, solar radiation was ~~woken~~ weak during the nighttime, which resulted in the accumulation of $NO_3$ due to the cease of photolysis of $NO_3$ (Rollins et al., 2012; Chen et al., 2020). AOC contributed by $O_3$ was negligible, owing to the relatively low concentration of alkenes at the monitoring site (Fig.1 and Table ~~2~~3), since $O_3$ contributed to the oxidation capacity through alkenes ozonolysis (Xue et al., 2016). In summary, the OH radical dominated the AOC ~~in Xiamen~~, and it was necessary to further explore the partitioning of OH reactivity among different precursor groups.

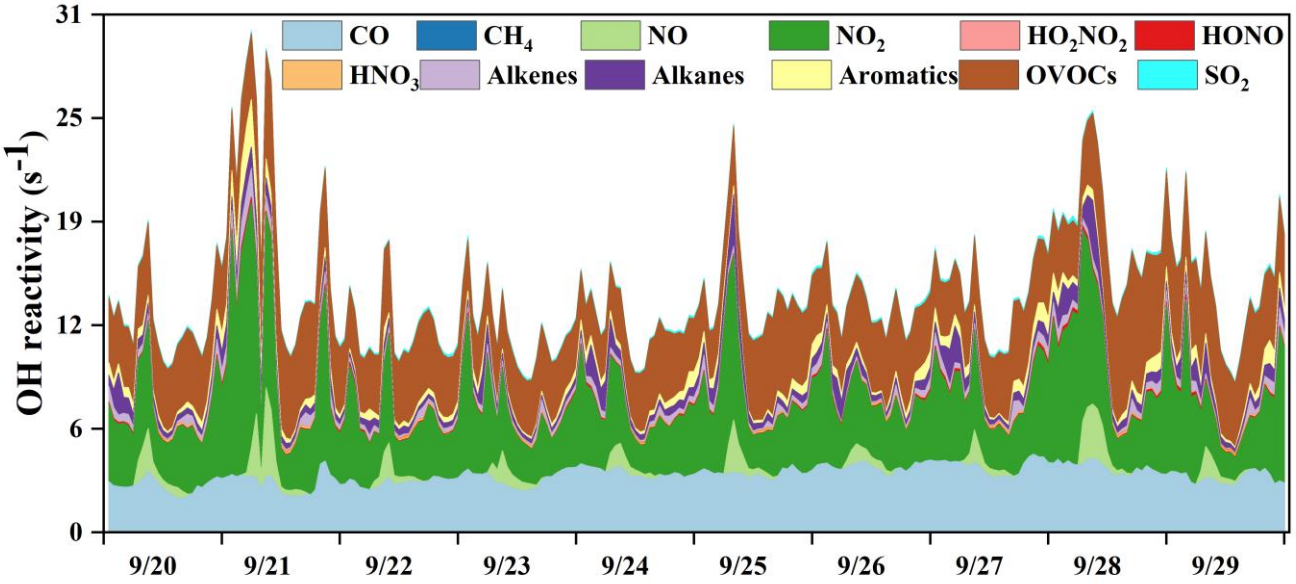


**Figure 4. Time series of model-calculated OH reactivity and its partitioning to the major reactants in Xiamen during 20-29 Sep. 2019.**

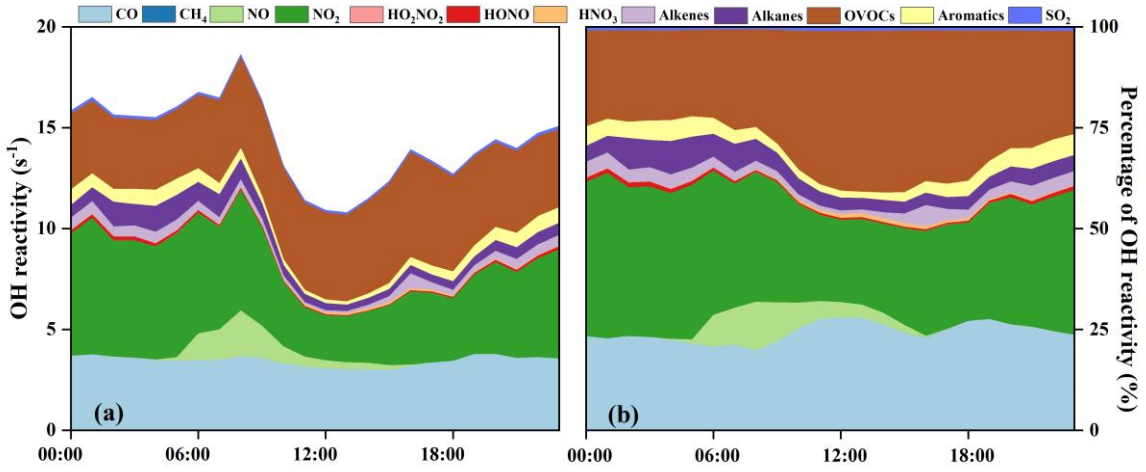

**Figure 5. (a) Diurnal patterns and (b) percentage of model-calculated OH reactivity and its partitioning to the major reactants**

The OH reactivity is an indicator for the OH chemical loss frequency, computed as the reaction rates of OH with CO, NOx, $SO_2$, HONO, $HNO_3$, $HO_2NO_2$, and VOCs (Whalley et al., 2016; Chen et al., 2020). ~~Zhu et al. (2020) found that unmeasured species and unknown secondary products contributed considerably to the actual OH reactivity.~~ Time series and diurnal patterns of model-calculated OH reactivity as well as its partitioning to the major reactants during the episode are shown in Fig. 4 and Fig. 5. The OH reactivity reached the peak (18.6±4.8 $s^{-1}$) at around 8:00 LT, mainly caused by the reaction of OH with NOx, since vehicles exhaust ~~emitted~~ large amounts of NOx during rush hours. The average daily OH reactivity was 14.4±3.83 $s^{-1}$, which was much lower than those in some polluted regions in Santiago (42 $s^{-1}$) and the PRD (50 $s^{-1}$), comparable to that at a rural site in Nashville (11 $s^{-1}$), but higher than that at a mountain site in Pennsylvania (6 $s^{-1}$) (Elshorbany et al., ~~2008~~2009; Lou et al., 2010a; Lou et al., 2010b; Kovacs et al., 2003; Ren et al., 2005). Figure 5 shows the diurnal variations and percentage of model-calculated OH reactivity to the major reactants during the episode. The OH reactivity exhibited a morning peak caused by the reactions of NO with OH, which should be ascribed to the freshly emitted urban plumes. Anymore, OVOCs showed high fractions at around 12:00-18:00 LT, which were mainly owing to the transport of the regional air masses containing the abundant OVOCs, as well as the oxidation effection by strong photochemical process. As shown in Fig. 5b, OVOCs (30±8 %) ~~and~~ , $NO_2$ (29±8%) and CO (25±5%), were the dominant contributors to OH reactivity, followed by ~~CO (25±5%),~~ alkanes (5±3%), aromatics (3±2%), alkenes (3±1%), and NO (2±4%). The high fraction of OVOCs and $NO_2$ in OH reactivity indicated the high aged degree of air mass and the intensive $NO_x$ emissions during the observation period, respectively (Li et al., 2018). However, the fraction of CO to OH reactivity at our observation site was higher than that at an urban site in Los Angeles (Hansen et al., 2021), a rural site in Hong Kong (Li et al., 2018), and a mountain site in Colorado (Nakashima et al., 2014), comparable to that at the urban site of Shanghai (Zhang et al., 2021a), which could be attributed to the abundant CO in our observation site. CO mainly comes from vehicle exhaust and the combustion of fossil fuels, and the observation site is a city with high density vehicles. Meanwhile, this pollution event was under the influence of the WPSH, which promoted the formation and accumulation of pollutants. The partitioning of OH reactivity elucidated the inherent photochemical processes and major reactants in Southeast China. High OH reactivity of OVOCs, $NO_2$, and CO would promote the production of ROx radical. Therefore, the investigation of detailed chemical budget of the ROx, recycling, and termination reaction is meaningful to figure out the complex atmospheric photochemistry (Li et al., 2018; Lou et al., 2010b).

### 3.2.2 Radical chemistry

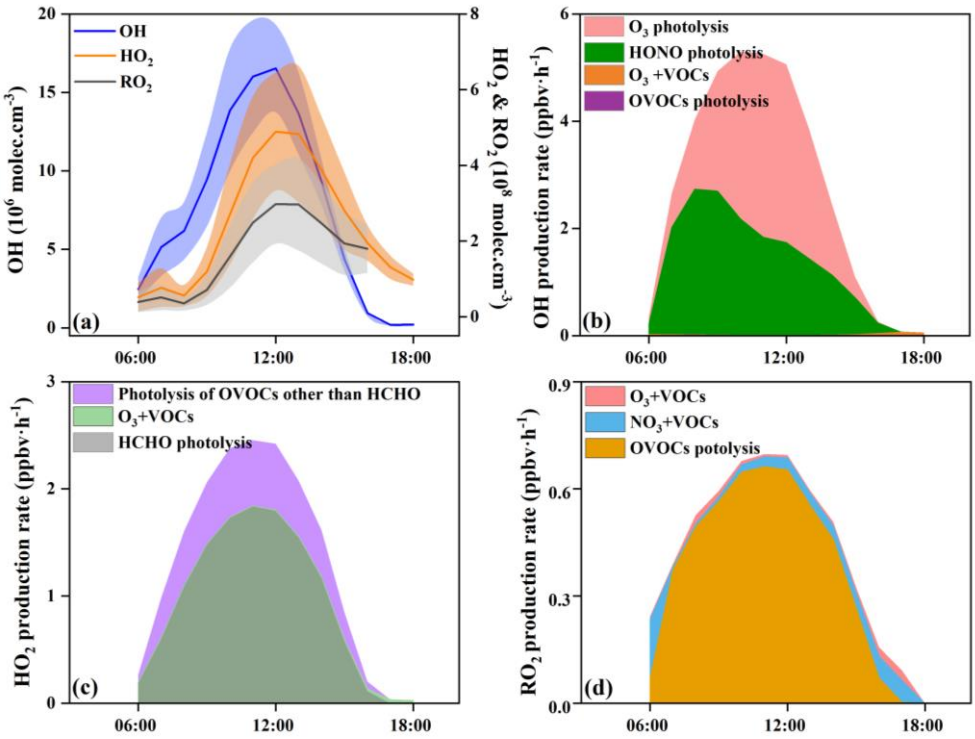


**Figure 6. Model-simulated daytime average diurnal variations in (a) OH, $HO_2$, and $RO_2$ concentrations, and average primary production rates of (b) OH, (c) $HO_2$, and (d) $RO_2$ during 20-29 Sep. 2019 in Xiamen.**

With the influence of NOx and VOCs, ROx radicals (OH, $HO_2$, and $RO_2$) undergo efficient recycling and produce secondary pollutants, such as $O_3$ and OVOCs (Sheehy et al., 2010). Figure 6 shows the model-simulated OH, $HO_2$, and $RO_2$ concentrations and their primary sources. The detailed time series of ROx concentrations and chemical budget are summarized in Fig. ~~S4~~S3. Figure 6a shows the diurnal variations of the simulated OH, $HO_2$, and $RO_2$. The maximum daily values of OH, $HO_2$, and $RO_2$ concentrations were $2.4\times10^7$, $7.9\times10^8$ and $4.7\times10^8$ molecules·cm$^{-3}$, with the daytime average concentrations of $7.4\times10^6$, $2.4\times10^8$ and $1.7\times10^8$ molecules·cm$^{-3}$, respectively. Model-predicted concentrations of OH in Xiamen were higher than that in ~~the~~ the Yellow River Delta (an oil field with high VOCs emission), while the concentrations of $HO_2$ and $RO_2$ showed ~~a~~ reverse trends (Chen et al., 2020). The ROx recycling of OH→$RO_2$ was mainly controlled by the reaction of OH+VOCs, and the $RO_2$→$HO_2$ and $HO_2$→OH depended on the reactions with NO (Fig.7). Combined with the ratio of VOCs/NOx (1.1±0.4), it was convinced that NOx would not be the limiting factor in the radical recycling processes. Hence, efficient conversions of radical propagation of $RO_2$+NO→$HO_2$ and $HO_2$+NO→~~HO~~ OH were expected, and OH+VOCs→$RO_2$ reaction was the rate-depended step of the radical recycling in our study. The detailed radical chemistry would be further discussed as follows.

Figure 6b shows the daytime average diurnal variations of primary OH sources. HONO photolysis reached the maximum of 2.7 ppb $h^{-1}$ at around 8:00 LT, which occupied 56±19% of the total OH primary production rates. The second source of OH primary production was $O_3$ photolysis (42±21%), and the percentages of $O_3$+VOCs and OVOCs photolysis were minor. The highest HONO photolysis rate appeared in the morning rush hour, suggesting the influence ~~from~~ of vehicle emissions and nocturnal accumulation of HONO (Hu et al., 2020~~a~~). Considering the radical recycling ~~of radicals~~, the reaction of $HO_2$+NO (8.0±6.2 ppb $h^{-1}$) dominated the total production of OH (Fig. ~~S4a~~S3a). Meanwhile, OH-initiated oxidations of VOCs (4.9±3.3 ppb $h^{-1}$) consumed OH most during the daytime, followed by OH+CO (2.6±1.9 ppb $h^{-1}$), OH+$NO_2$ (2.4±1.1 ppb $h^{-1}$), OH+NO (0.6±0.3 ppb $h^{-1}$), and OH+$O_3$ (0.2±0.1 ppb $h^{-1}$).

In this study, HCHO photolysis was identified as the most important source for $HO_2$ primary formation, with an average production rate of 1.1±0.6 ppb $h^{-1}$ (Fig.6c), followed by the other OVOCs photolysis (0.4±0.2 ppb $h^{-1}$). The rate of OVOCs photolysis in Xiamen was much lower than that in some megacities, such as Beijing (Liu et al., 2012) and Hong Kong (Xue et al., 2016). The reaction of OH+CO (2.6±2.2 ppb $h^{-1}$) and $RO_2$+NO (2.5±1.5 ppb $h^{-1}$) were also important sources of $HO_2$ (Fig. ~~S4b~~S3b). The main sink~~s~~ of $HO_2$ ~~were~~ was $HO_2$+NO (7.9±6.2 ppb $h^{-1}$), while the loss rates of $HO_2$+$HO_2$ and $HO_2$+$RO_2$ were negligible.

In Fig. 6d, OVOCs photolysis contributed most to primary $RO_2$ production with a rate of 0.5±0.2 ppb $h^{-1}$, accounting for 85±20% of total $RO_2$ primary production. The reaction~~s~~ of unsaturated VOCs and $NO_3$ ~~were~~ was the second important source, accounting for 11±18 % of the total primary $RO_2$. The radical recycling rate of OH+VOCs was 8.4 times higher than the sum of $RO_2$ primary production. The consumption reaction of $RO_2$ was mainly caused by $RO_2$+NO (3.7±2.9 ppb $h^{-1}$), and the cross-reactions by ROx themselves were limited.

The daytime average ROx budget and its recycling were also demonstrated (Fig. 7). For the ROx primary sources, the photolysis of HONO (33±14%), $O_3$ (25±13%), HCHO (20±5%) and other OVOCs (17±2%) were the major contributors. For ROx recycling, CO and VOCs reacted with OH producing $HO_2$ and $RO_2$ with the average rates of 4.0 and 4.4 ppbv $h^{-1}$, respectively. $RO_2$+NO and $HO_2$+NO enhanced the production of RO (3.6 ppbv $h^{-1}$) and OH (7.9 ppbv $h^{-1}$), with $O_3$ formed as a by-product. For the termination processes, the ~~reactions~~ reaction rates of ROx ~~with~~ and NOx were approximately 2-5 times faster than the cross-~~reactions~~ reaction rates of ROx.

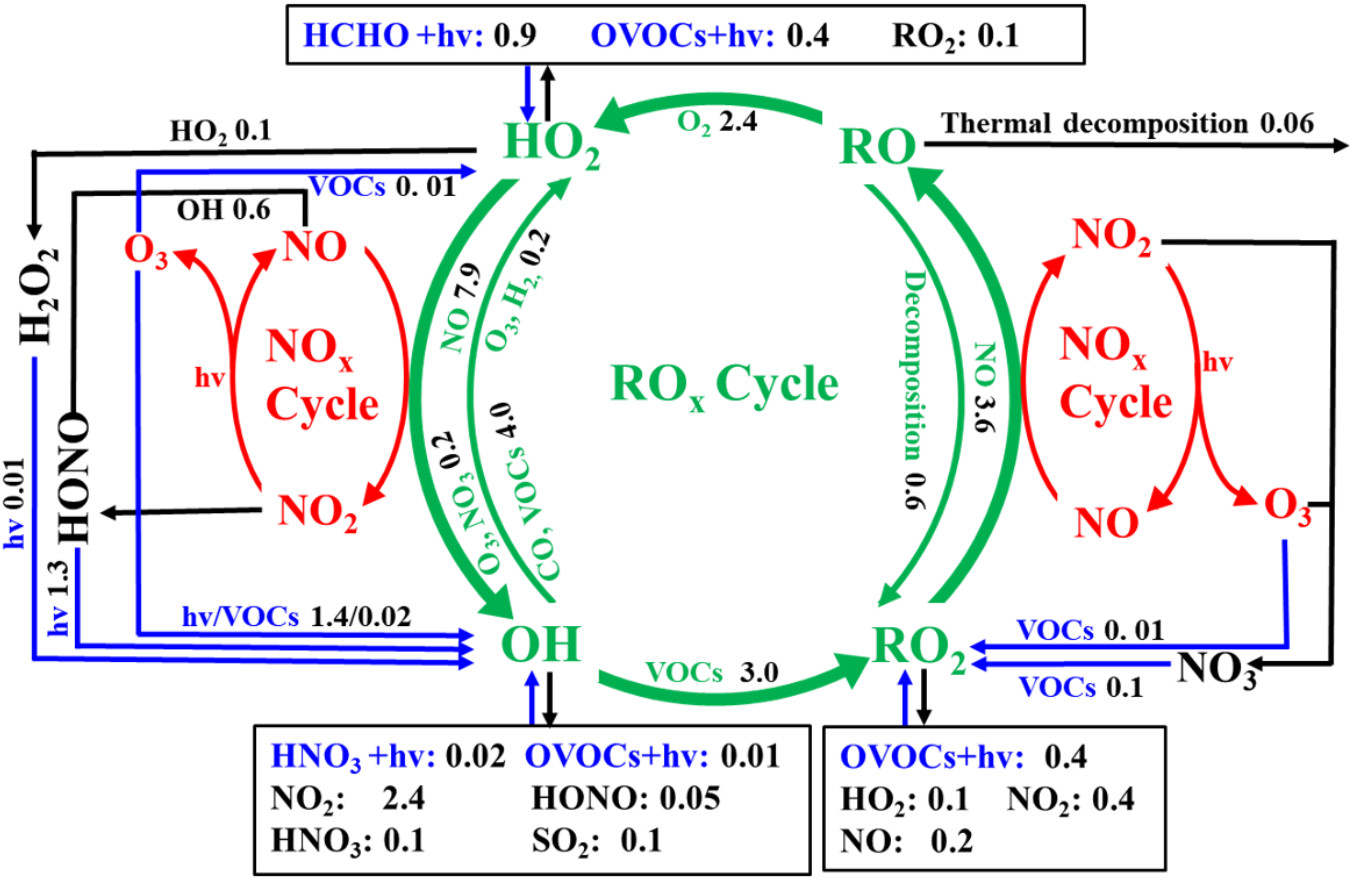


**Figure 7. Daytime ROx budget during 20-29 Sep. 2019 in Xiamen. The unit is parts per billion per hour. The blue, black, and green lines and words indicate the production, destruction, recycling pathways of radicals, respectively.**

## 3.3 $O_3$ formation mechanism

### 3.3.1 Chemical budget and sensitivity analysis of $O_3$ production

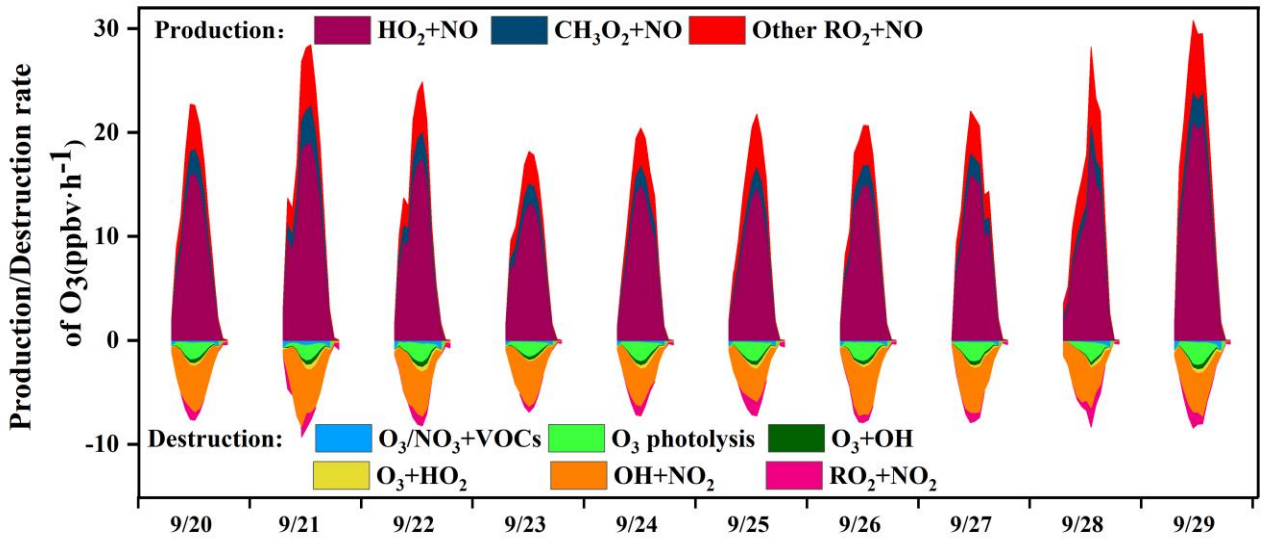


**Figure 8. Time series of model-simulated $O_3$ chemical budgets during 20-29 Sep. 2019 in Xiamen.**

The in situ $O_3$ production mechanism was examined, and the detailed reaction weights ~~are~~ were

shown in Fig. 8. The daytime rate of $HO_2$+NO was 7.9±6.2 ppb $h^{-1}$, accounting for 68±4% of the total $O_3$ production. This result was consistent with that in section 3.2.2. The OH radical was the initiator of $O_3$ photochemical ~~$O_3$~~ formation, and the ~~main~~ source~~s~~ of OH from $HO_2$+NO was also the dominant pathway to produce $O_3$ (Liu et al., 2020c). The second pathway of $O_3$ production was $RO_2$+NO (3.6±2.0 ppb $h^{-1}$). The reaction of $RO_2$+NO contained more than 1000 types of $RO_2$ radicals, and the pathway of $CH_3O_2$+NO (34±6%) contributed ~~the~~ mostly among them. In contrast, the contributors of $O_3$ destruction were OH+$NO_2$ (61±18%), followed by $O_3$ photolysis (18±9%), $RO_2$+$NO_2$ (9±10%), $O_3$+$HO_2$ (4±4%), and $O_3$+OH (4±2%), while the other pathways of $O_3$+VOCs as well as $NO_3$+VOCs~~,~~ contributed limitedly. In addition, the net $O_3$ production (9.1±5.7 ppb $h^{-1}$) in Xiamen was ~2-5 times lower than that derived from the metropolis of Shanghai (26 ppb $h^{-1}$), Lanzhou (23 ppb $h^{-1}$) and Guangzhou (50 ppb $h^{-1}$), reflecting the influence of $O_3$ precursor~~s~~ emissions and photochemical conditions (Xue et al., 2014).

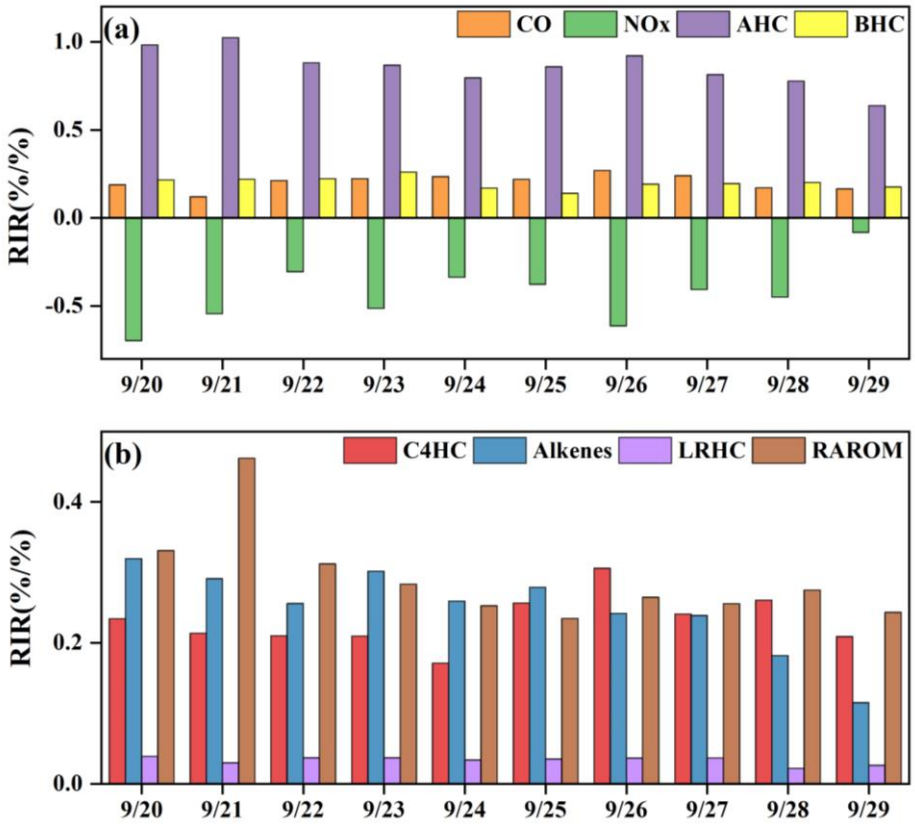


**Figure 9. The model-calculated RIRs for (a) major $O_3$ precursor groups and (b) the AHC sub-groups during high $O_3$ daytime (06:00-18:00 LT) (AHC: anthropogenic hydrocarbons; BHC: biogenic hydrocarbons; RAROM: aromatics except for benzene; LRHC: low reactivity hydrocarbons; C4HC: alkenes, and alkanes with ≥4 carbons).**

In this study, we also calculated the relative incremental reactivity (RIR) to diagnose the sensitivity of $O_3$ formation to its precursors. Figure 9 shows the RIR values for major groups of $O_3$ precursors. Around 50 types of VOCs were classified as anthropogenic hydrocarbons (AHC), and the isoprene was categorized into biogenic hydrocarbons (BHC)~~, with~~. Moreover, AHC further divided into four groups of

reactive aromatics (RAROM, including aromatics except for benzene), low reactivity hydrocarbons (LRHC, including ethane, acetylene, propane, and benzene), alkenes, and alkanes with ≥4 carbons (C4HC). The in situ $O_3$ production was highly VOCs-sensitive, especially for AHC-sensitive (0.63–1.02 %/%) (Fig. 9a), followed by CO (0.17–0.27 %/%) and BHC (0.14–0.26 %/%), indicating the impacts from anthropogenic activities and flourishing vegetation emissions (Liu et al., 2020a; Lin et al., 2020). The RIRs were NOx-negative ranging from -0.70 to -0.08. As shown in Fig. 9b, the contributors of AHC sub-groups to RIRs were RAROM (0.24–0.46 %/%), C4HC (0.17–0.30 %/%), alkenes (0.11–0.32 %/%), and LRHC (0.03–0.04 %/%). Therefore, the reduction of aromatics, alkenes, and ~~longer~~ alkanes with ≥4 carbons effectively decreased $O_3$ production, and the reduction of NOx might aggravate $O_3$ pollution.

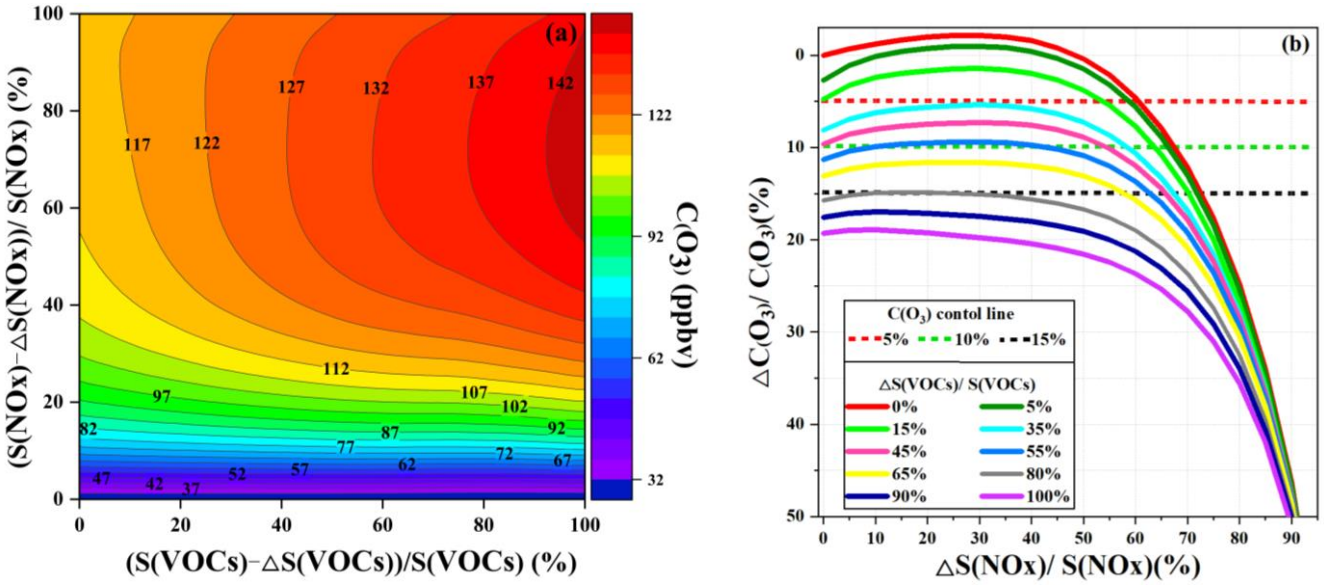


**Figure 10 (a) Isopleth diagrams of modeled $O_3$ production potential ($C(O_3)$) on S(VOCs) and S(NOx) remaining percentages (i.e., (S(VOCs)-S(VOCs))/(S(VOCs)) and (S (NOx)-S(NOx))/(S(NOx)); (b) Relationship of $C(O_3)$ increment percentage ($\triangle C(O_3)/C(O_3)$) with S(NOx) and S(VOCs) reduction percentages (△S(NOx)/S(NOx) and △S(VOCs)/S(VOCs)). Note: $C(O_3)$, S(NOx), and S(NOx) represent the concentrations of corresponding pollutants.**

In order to investigate the $O_3$ control strategies ~~in the relatively clean coastal city~~during this multi-day $O_3$ pollution event, the scenario analysis with reduction by 0-100% at intervals of 5% for the reduction of anthropogenic VOCs (△S(VOCs)/S(VOCs) and NOx (△S(NOx)/S(NOx)) were conducted using the OBM-MCM. According to the Empirical Kinetic Modeling Approach (EKMA) and scenario analysis, $O_3$ formation was in the NO-titration regime (Fig. 10), in accordance with those of RIR analysis, which meant VOCs should be reduced to effectively control $O_3$ during the $O_3$ pollution event. The maximum value of MDA8h $O_3$ during the monitoring period was 85 ppbv, exceeding the national air quality standard of 75 ppbv for $O_3$ by 13%. Hence, the $O_3$ reductions of 5%, 10%, and 15% were set to discuss the reduction

schemes of anthropogenic VOCs and NOx. As shown in Fig. 10b, achieving the 5% control target were 1) S(VOCs) is reduced by 15%, while S(NOx) remains unchanged; 2) S(VOCs) is reduced larger than 35%; 3) S(NOx) reduction is higher than 60%. The first scenario of just reducing VOCs emission was the most cost-efficient way for short-term or emergency control of $O_3$. However, NOx, as important precursors of $PM_{2.5}$, need to be reduced according to the long-term multi-pollutant control air quality improvement plan in China, thus the second scenario is a more practical and reasonable way to control air pollution. ~~In addition, t~~The 10% of $O_3$ control target was achieved by the 45% reduction of S(VOCs), and the S(NOx) keeps original emission. In view of the long-term control strategy of NOx and VOCs, S(VOCs) reduced by 55% and 80% could decrease 10% and 15% $O_3$ concentrations, respectively. Although VOCs and NOx control measures were drastically implemented, it is still challenging to achieve the 15% $O_3$ control goals in urban areas with relatively low precursor emissions. As the episode is a typical pollution process in the coastal region, the research results might act as reference for the policy makers. Meanwhile, as the $O_3$ sensitivity changed under the implementation of control measures, it is necessary to adjust timely the reduction of VOC and NOx policies.

### 3.3.2 $O_3$ from local photochemical production and regional transport

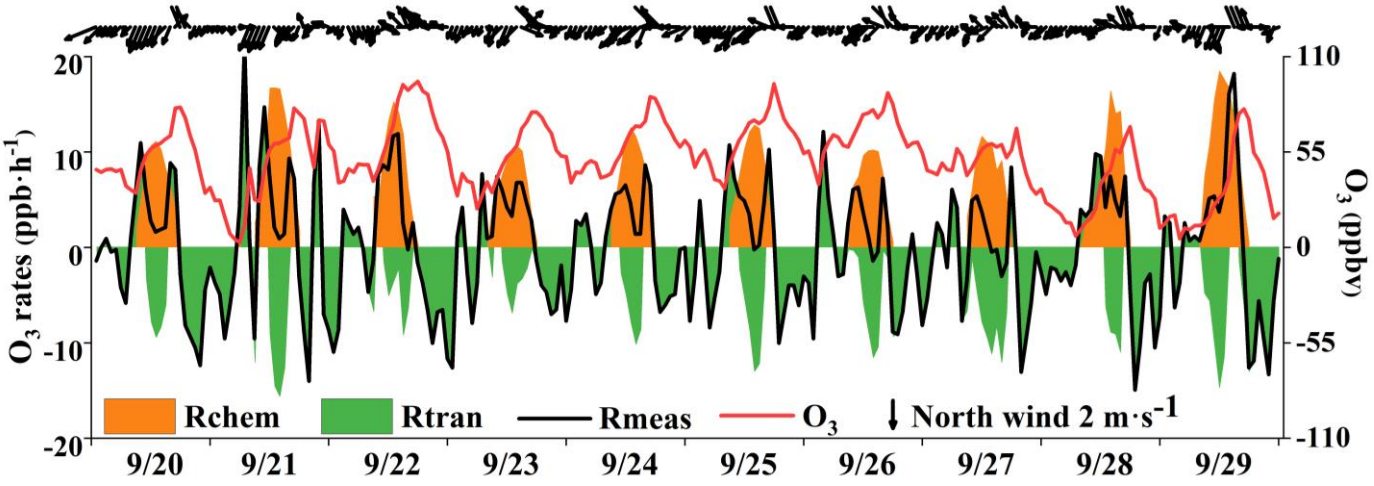


**Figure 11. $O_3$ accumulation and contributions from local photochemical production and regional transport, and Rchem, Rtran, and Rmeas in figure caption represent local $O_3$ photochemical production, regional transport and observed $O_3$ formation rate, respectively.**

Previous studies have found that the variation of $O_3$ mixing ratios was mainly influenced by chemical and physical processes (Xue et al., 2014; Tan et al., 2018). Figure 11 shows the time series of $O_3$ accumulation and contributions from local photochemical production and regional transport. The observed rate of change in $O_3$ (Rmeas) was calculated by the derivative of the observed $O_3$ concentrations (Rmeas=d($O_3$)/dt). The local $O_3$ production (Rchem) was calculated by Equation 3, and computed hourly by the OBM as described in Section 2.2. The physical processes (Rtran)~~regional transport (Rtran)~~ ~~was~~

were calculated by the equation of Rtran=Rmeas−Rchem, including horizontal and/or vertical transport, dry deposition dilution mixing, and so on. Many studies showed that the impacts of dry deposition were minor, thus the differences between observed $O_3$ changes and local $O_3$ production were mainly caused by the regional transport (note that the effect of atmospheric mixing was also included in this term), which could be treated as regional transport and could reasonably quantify the contributions of regional transport at our observation site (Zhang et al., 2021; Chen et al., 2020). The positive values of Rtran represented the $O_3$ import of regional transport, while the negative values indicated the $O_3$ export and deposition. We quantified the contributions of local photochemical formation and regional transport to the observed $O_3$, and figured out the reasons for the $O_3$ pollution process.

As shown in Fig. 11, two regular $O_3$ import phenomenon with positive values of Rtran were observed, and the curve of the Rmeas showed the "M" trend during the daytime. The first transient intense $O_3$ import happened in the early morning (at around 6:00-9:00), leading to a rapid increase in $O_3$ concentration, which was mainly attributed to the residual ozone from the day before. -The $O_3$ export was remarkable at around 10:00-16:00, indicating the potential impacts on air quality in downwind areas. Generally, the maximum daily value of $O_3$ at this observation site– appeared at around 15:00 LT without regional transport (Wu et al., 2019). In Figure 11, we found that the $O_3$ concentrations showed two peaks at around 15:00 and 17:00 LT, and $O_3$ concentrations rose slowly, or even decreased firstly and then increased between the two peaks. Under these circumstances, the local photochemical production kept producing $O_3$, but the decreased $O_3$ concentrations could be attributed to the favorable atmospheric conditions in diluting pollutants ($O_3$ export). When the near-surface wind direction changed from northeast to southeast, the second $O_3$ import phenomenon occurred in the afternoon (16:00-19:00 LT) in four days (20, 25 27 and 29 Sep.). Due to the persistence of Rtran in the afternoon, the daily maximum $O_3$ values appeared at around 17:00 LT. Under the conditions of southeast wind direction, downtown area with high density vehicles would make $O_3$ and its precursors transmitting to our observation site, consistent with the diurnal patterns of $NO_2$, OVOCs, alkanes, and aromatic in the early morning and afternoon (Fig. 2) to match with the "M" trend of Rmeas. This result indicated that the sudden changes of near-surface winds were corresponding to the variation in the transport of the urban plume.

According to ~~photochemical parameters including UV, $JNO_2$, $JO^1D$ and~~ the synoptic situations and meteorological parameters (Fig. 1, Fig. ~~S5~~ S4 and Fig.12), the environmental conditions also favored the $O_3$ pollution process during the observation periods. The contribution of Rchem (daily maximum: ranged from 10.2 to 19.1 ppb $h^{-1}$) during the daytime was observed (Fig.11). In Fig. ~~S5abc~~S4abc, the monitoring

site was continuously affected by the northerly ~~$O_3$ polluted~~ airflow with high $O_3$ and its precursors (from an industrial city adjacent to Xiamen of Quanzhou or polluted regions of Yangtze River Delta~~3~~), due to the typhoon 'Tapah' from 20 to 22 Sep. 2019. The transport of $O_3$ import appeared on 21 Sep. (7.1±7.0 ppb $h^{-1}$), which resulted in the accumulation of $O_3$ (the MDA8h $O_3$: 85 ppbv) on 22 Sep. When the influence of typhoon disappeared, the direction of airflow turned from northerly into southwest with humid and warm at 500hPa (Fig. ~~S5d~~S4d), the surface wind on Sep. 23 was affected by the control of the cold northerly airflow (Fig. ~~S5ef~~S4ef). Meteorological conditions including continental high pressure during 23 to 27 Sep. were favorable to the accumulation of air pollutants (Fig. 12). The isoline of 5880 gpm moving from north to the Yangtze River (Fig. 12a,b) indicated the strengthened subtropical high pressure during 23-27 Sep. 2019, which carried high temperature, low RH, and stagnant weather conditions, and the transport rate of $O_3$ export (5.4±3.4 ppb $h^{-1}$) on 24-26 Sep. was lower than that on other days (6.3±4.0 ppb $h^{-1}$). Favorable meteorological conditions significantly affected the formation and accumulation of $O_3$, and we chose five meteorological parameters (i.e. UV, T, RH, P and WS) to quantify the complex nonlinear relationships between $O_3$ and its influencing factors based on a generalized additive model (GAM) (Hua et al., 2021). Table S3 showed that the factors had significant non-linear impacts on $O_3$ concentration changes at the level of P-value<0.01 and degrees of freedom>1, indicating that each influencing factor has statistical significance as an explanatory variable. According to the F-values reflecting the importance of the influencing factors, the orders of the explanatory variables were RH (40.1) > WS (26.9) > T (10.9) > P (3.9) > UV (3.0). Response curves of $O_3$ concentration to explanatory factors are presented in Fig. 13. The $O_3$ concentration showed a remarkable upward trend until the UV increased to 17 $W \cdot m^{-2}$, then changed little with the fluctuation of UV (Fig. 13a). In previous studies, UV had a significant positive correlation with $O_3$ concentrations (Ma et al., 2020), and these results showed the regional transport impacts on $O_3$ formation in our study. The RH and T had negative and positive correlations with $O_3$ concentrations, respectively (Fig. 13b and Fig. 13c). The increase of wind speed was favorable for $O_3$ regional transport (Fig. 13d). The influence of atmospheric pressure on $O_3$ seemed to be irregular and minor, which could be ignored (Fig. 13e). Hence, under the combined effects of ~~stable~~ favorable ~~atmospheric~~ photochemical reaction conditions and strengthened WPSH, the MDA8h $O_3$ exceeded the standard of 75 ppbv during 24-26 Sep. Previous studies had found that severe multi-day $O_3$ pollution appeared under the WPSH control (Wang et al., 2018a). Overall, the results indicate that the three conditions of local photochemical production ~~and~~, synoptic situations ~~caused high $O_3$ concentrations,~~ and regional transport played very important roles in the pollution event~~aggravated~~

~~the $O_3$ pollution process~~.

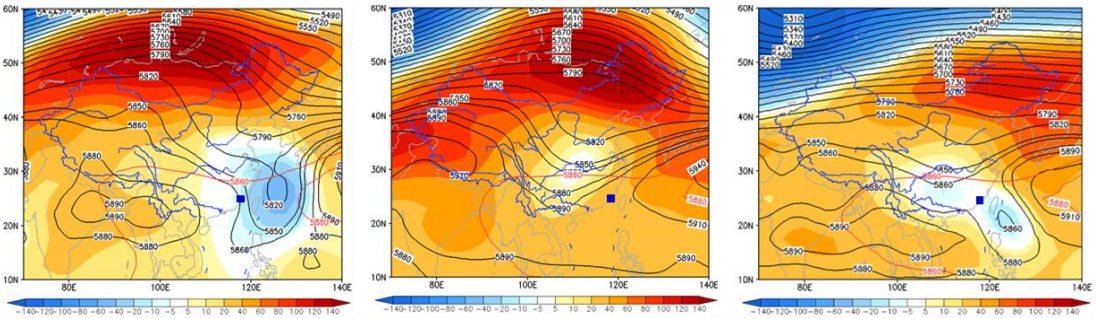


**Figure 12. Synoptic situations of continental high pressure from 20 to 29 Sep. 2019. The gradient color area indicates the WPSH over the map and the contour line was from the characteristic isoline of 5880 gpm to the center isoline of 5920 gpm. The blue square is the study site.**

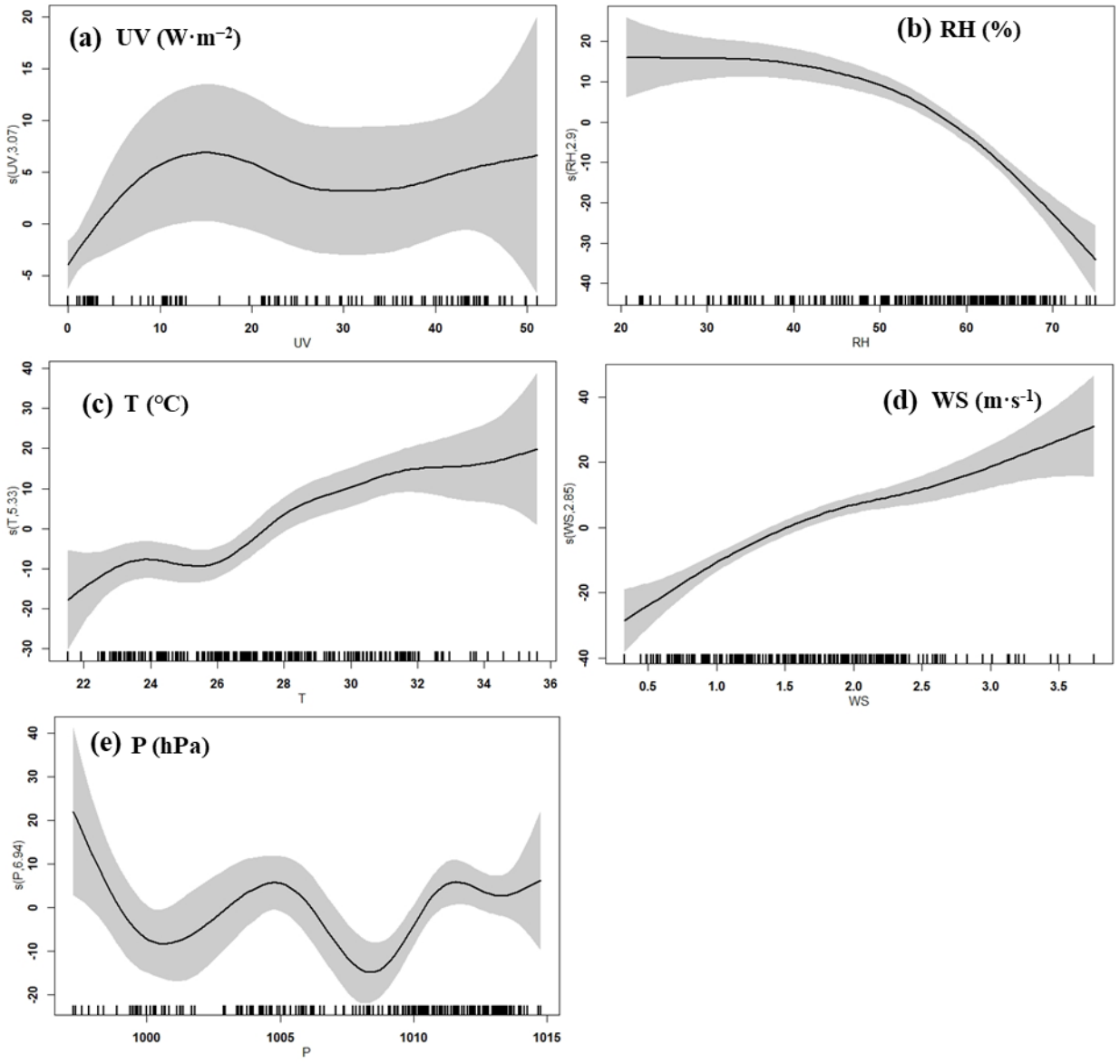

**Figure 13. Response curves in GAM model of $O_3$ concentration to changes in (a) ultraviolet radiation (UV), (b) relative humidity (RH), (c) temperature (T), (d) wind speed (WS), and (e) pressure (P). The y-axis is the smoothing function values. The x-axis is the influencing factor; the vertical short lines represent the concentration distribution characteristics of the explanatory variables; the shaded area around the solid line indicates the 95% confidence interval of $O_3$ concentration.**

## 4 Conclusions

In the present study, we analyzed a typical high $O_3$ event during 20-29 Sep. 2019 in a coastal city of Southeast China. We clarified the characteristics of AOC, OH reactivity, and radical chemistry, as well as $O_3$ formation mechanisms using the OBM-MCM model. The predominant oxidant for AOC during the daytime and nighttime was the OH and $NO_3$, respectively. During the period of $O_3$ pollution process, OVOCs, $NO_2$, and CO consumed OH mostly. Meanwhile, the photolysis of HONO, $O_3$, HCHO, and other OVOCs were ~~the most important~~ major ~~primary~~ sources of ROx, which played the initiation roles in atmospheric oxidation processes. The radical termination reactions were governed by cross-reactions between ROx and NOx. The RIRs and EKMA results showed that the $O_3$ formation in autumn in the coastal city was VOCs-sensitive, and the VOCs were the limited factor of radical recycling and $O_3$ formation. The reduced emissions of aromatics, alkenes, and ~~long-chain~~ alkanes with ≥4 carbons were benefit for ozone pollution control. The three conditions of local photochemical production ~~and,~~ synoptic situations ~~caused the high concentrations of $O_3$,~~ and ~~the~~ regional transport played very important roles in the pollution event~~aggravated the pollution of ozone~~. Overall, the results clarified the $O_3$ pollution process with relatively low local precursor emissions, and implied the fact that $O_3$ pollution control in coastal cities needs to be further studied.

## Authorship Contribution Statement

Taotao Liu and Youwei Hong contributed equally to this work. Jinsheng Chen and Likun Xue designed and revised the manuscript. Taotao Liu collected the data, contributed to the data analysis. Taotao Liu and Youwei Hong performed chemical modeling analyses of OBM-MCM and wrote the paper. Jinsheng Chen supported funding of observation and research. Lingling Xu, Mengren Li, Chen Yang, Yangbin Dan, Yingnan Zhang, and Min Zhao contributed to discussions of results. Zhi Huang and Hong Wang provided meteorological conditions in Xiamen.

## Acknowledgment

This study was funded by the Cultivating Project of Strategic Priority Research Program of Chinese Academy of Sciences (XDPB1903), the FJIRSM&IUE Joint Research Fund (RHZX-2019-006), the Center for Excellence in Regional Atmospheric Environment, CAS (E0L1B20201), the Xiamen Youth Innovation Fund Project (3502Z20206094), the foreign cooperation project of Fujian Province (2020I0038) and Xiamen Atmospheric Environment Observation and Research Station of Fujian Province.

## Reference:

Acker, K., Möller, D., Wieprecht, W., Auel, R., Kalaß, D., and Tscherwenka, W.: Nitrous and nitric acid measurements inside and outside of clouds at Mt. Brocken, Water Air Soil Pollut., 130, 331–336, 2001.

Chang, L., Xu, J., Tie, X., and Gao, W.: The impact of Climate Change on the Western Pacific Subtropical High and the related ozone pollution in Shanghai, China, Sci Rep, 9, 16998, 10.1038/s41598-019-53103-7, 2019.

Chen, T., Xue, L., Zheng, P., Zhang, Y., Liu, Y., Sun, J., Han, G., Li, H., Zhang, X., Li, Y., Li, H., Dong, C., Xu, F., Zhang, Q., and Wang, W.: Volatile organic compounds and ozone air pollution in an oil production region in northern China, Atmos. Chem. Phys., 20, 7069-7086, 10.5194/acp-20-7069-2020, 2020.

Deng, J., Guo, H., Zhang, H., Zhu, J., Wang, X., and Fu, P.: Source apportionment of black carbon aerosols from light absorption observation and source-oriented modeling: an implication in a coastal city in China, Atmospheric Chemistry and Physics, 20, 14419-14435, 10.5194/acp-20-14419-2020, 2020.

Edwards, P. M., Brown, S. S., Roberts, J. M., Ahmadov, R., Banta, R. M., Degouw, J. A., Dubé, W. P., Field, R. A., Flynn, J. H., Gilman, J. B., and Graus, M.: High winter ozone pollution from carbonyl photolysis in an oil and gas basin, Nature, 514, 351, https://doi.org/10.1038/nature13767, 2014.

Edwards, P. M., Young, C. J., Aikin, K., deGouw, J., Dubé, W. P., Geiger, F., Gilman, J., Helmig, D., Holloway, J. S., Kercher, J., Lerner, B., Martin, R., McLaren, R., Parrish, D. D., Peischl, J., Roberts, J. M., Ryerson, T. B., Thornton, J., Warneke, C., Williams, E. J., and Brown, S. S.: Ozone photochemistry in an oil and natural gas extraction region during winter: simulations of a snow-free season in the Uintah Basin, Utah, Atmos. Chem. Phys., 13, 8955–8971, https://doi.org/10.5194/acp13-8955-2013, 2013.

Eisele, F. L., Mount, G. H., Tanner, D., Jefferson, A., Shetter, R., Harder, J. W., and Williams, E. J.: Understanding the production and interconversion of the hydroxyl radical during the Tropospheric OH Photochemistry Experiment, J. Geophys. Res., 102, 6457–6465, 1997.

Elshorbany, Y. F., Kurtenbach, R., Wiesen, P., Lissi, E., Rubio, M., Villena, G., Gramsch, E., Rickard, A. R., Pilling, M. J., and Kleffmann, J.: Oxidation capacity of the city air of Santiago, Chile, Atmos. Chem. Phys., 9, 2257–2273, https://doi.org/10.5194/acp-9-2257-2009, 2009.

Emmerson, K. M., Carslaw, N., and Pilling, M. J.: Urban Atmospheric Chemistry During the PUMA Campaign 2: Radical Budgets for OH, $HO_2$ and $RO_2$, J. Atmos. Chem., 52, 165-183, 10.1007/s10874-005-1323-2, 2005.

Fowler, D., Pilegaard, K., Sutton, M. A., Ambus, P., Raivonen, M., Duyzer, J., Simpson, D., Fagerli, H., Fuzzi, S., Schjoerring, J. K., Granier, C., Neftel, A., Isaksen, I. S. A., Laj, P., Maione, M., Monks, P. S., Burkhardt, J., Daemmgen, U., Neirynck, J., Personne, E., Wichink-Kruit, R., Butterbach-Bahl, K., Flechard, C., Tuovinen, J. P., Coyle, M., Gerosa, G., Loubet, B., Altimir, N., Gruenhage, L., Ammann, C., Cieslik, S., Paoletti, E., Mikkelsen, T. N., Ro-Poulsen, H., Cellier, P., Cape, J. N., Horváth, L., Loreto, F., Niinemets, Ü., Palmer, P. I., Rinne, J., Misztal,

P., Nemitz, E., Nilsson, D., Pryor, S., Gallagher, M. W., Vesala, T., Skiba, U., Brüggemann, N., Zechmeister-Boltenstern, S., Williams, J., O'Dowd, C., Facchini, M. C., de Leeuw, G., Flossman, A., Chaumerliac, N., and Erisman, J. W.: Atmospheric composition change: Ecosystems–Atmosphere interactions, Atmos. Environ., 43, 5193-5267, 10.1016/j.atmosenv.2009.07.068, 2009.

George, L. A., Hard, T. M., and O'Brien, R. J.: Measurement of free radicals OH and $HO_2$ in Los Angeles smog, J. Geophys. Res., 104, 11643–11655, 1999.

Geyer, A., Alicke, B., Konrad, S., Schmitz, T., Stutz, J., and Platt, U.: Chemistry and oxidation capacity of the nitrate radical in the continental boundary layer near Berlin, J. Geophys. Res., 106, 8013-8025, 10.1029/2000jd900681, 2001.

Gong, C., and Liao, H.: A typical weather pattern for the ozone pollution events in North China, Atmos. Chem. Phys., 10.5194/acp-2019-263, 2019.

Hofzumahaus, A., Rohrer, F., Lu, K. D., Bohn, B., Brauers, T., Chang, C. C., Fuchs, H., Holland, F., Kita, K., Kondo, Y., Li, X., Lou, S. R., Shao, M., Zeng, L. M., Wahner, A., and Zhang, Y. H.: Amplified Trace Gas Removal in the Troposphere, Science, 324, 1702–1704, 2009.

Hong, Z., MengzeLi, HongWang, LinglingXu, Hong, Y., Chen, J., Chen, J., Zhang, H., Zhang, Y., Wu, X., Hu, B., and Li, M.: Characteristics of atmospheric volatile organic compounds (VOCs) at a mountainous forest site and two urban sites in the southeast of China, Sci Total Environ, 10.1016/j.scitotenv.2018.12.132, 2019.

Hu B, Liu T, Yang Y, Hong Y, Li M, Xu L, Wang H, Chen N, Wu X, Chen J: Characteristics and Formation Mechanism of Surface Ozone in a Coastal Island of Southeast China: Influence of Sea-land Breezes and Regional Transport. Aerosol Air Qual. Res., 19(8):1734-1748, 2019.

Hu, B., Duan, J., Hong, Y., Xu, L., Li, M., Bian, Y., Qin, M., Fang, W., Xie, P., and Chen, J.: Exploration of the atmospheric chemistry of nitrous acid in a coastal city of southeastern China: Results from measurements across four seasons, Atmos. Chem. Phys. Discuss. [preprint], https://doi.org/10.5194/acp-2021-723, 2021.

Hu, B., Liu, T., Hong, Y., Xu, L., Li, M., Wu, X., Wang, H., Chen, J., and Chen, J.: Characteristics of peroxyacetyl nitrate (PAN) in a coastal city of southeastern China: Photochemical mechanism and pollution process, Sci Total Environ, 719, 137493, 10.1016/j.scitotenv.2020.137493, 2020.

Hansen R F, Griffith S M, Dusanter S, et al.: Measurements of Total OH Reactivity During CalNex-LA. J. Geophys. Res, Atmos, 126(11), e2020JD032988, 2021.

Jenkin, M. E., Saunders, S. M., Wagner, V., and Pilling, M. J.: Protocol for the development of the Master Chemical Mechanism, MCM v3 (Part B): tropospheric degradation of aromatic volatile organic compounds, Atmos. Chem. Phys., 3, 181–193, https://doi.org/10.5194/acp-3-181-2003, 2003.

Hansen R F, Griffith S M, Dusanter S, et al.: Measurements of Total OH Reactivity During CalNex-LA. J. Geophys. Res, Atmos, 126(11), e2020JD032988, 2021.

Hua, J., Zhang, Y., de Foy, B., Shang, J., Schauer, J. J., Mei, X., Sulaymon, I. D., and Han, T.: Quantitative estimation of meteorological impacts and the COVID-19 lockdown reductions on $NO_2$ and $PM_{2.5}$ over the Beijing area using Generalized Additive Models (GAM), J Environ Manage, 291, 112676, 10.1016/j.jenvman.2021.112676, 2021.

Jiang Y, Xue L, Gu R, Jia M, Zhang Y, Wen L, Zheng P, Chen T, Li H, Shan Y et al: Sources of nitrous acid (HONO) in the upper boundary layer and lower free troposphere of the North China Plain: insights from the Mount Tai Observatory. Atmos. Chem. Phys., 20(20):12115-12131, 2020.

Kanaya, Y., Cao, R. Q., Akimoto, H., Fukuda, M., Komazaki, Y., Yokouchi, Y., Koike, M., Tanimoto, H., Takegawa, N., and Kondo, Y.: Urban photochemistry in central Tokyo: 1. Observed and modeled OH and $HO_2$ radical concentrations during the winter and summer of 2004, J. Geophys. Res., 112, D21312, doi:10.1029/2007JD008670, 2007.

Kanaya, Y., Matsumoto, J., Kato, S., and Akimoto, H.: Behavior of OH and $HO_2$ radicals during the Observations at a Remote Island of Okinawa (ORION99) field campaign 2. Comparison between observations and calculations, J. Geophys. Res., 106, 24209–24223, 2001.

Kovacs, T. A., Brune, W. H., Harder, H., Martinez, M., Simpas, J. B., Frost, G. J., Williams, E., Jobson, T., Stroud, C., Young, V., Fried, A., and Wert, B.: Direct measurements of urban OH reactivity during Nashville SOS in summer 1999, J. of Environ. Monitor., 5, 68-74, 10.1039/b204339d, 2003.

Li, B., Ho, S. S. H., Gong, S., Ni, J., Li, H., Han, L., Yang, Y., Qi, Y., and Zhao, D.: Characterization of VOCs and their related atmospheric processes in a central Chinese city during severe ozone pollution periods, Atmos. Chem. Phys., 19, 617-638, 10.5194/acp-19-617-2019, 2019.

Li, N., He, Q., Greenberg, J., Guenther, A., Cao, J., & Wang, J., Liao H., Zhang Q.: Impacts of biogenic and anthropogenic emissions on summertime ozone formation in the Guanzhong Basin, China, Atmos. Chem. Phys., 2018a.

Li, Z., Xue, L., Yang, X., Zha, Q., Tham, Y. J., Yan, C., Louie, P. K. K., Luk, C. W. Y., Wang, T., and Wang, W.: Oxidizing capacity of the rural atmosphere in Hong Kong, Southern China, Sci Total Environ, 612, 1114-1122, 10.1016/j.scitotenv.2017.08.310, 2018.

Lin, H., Wang, M., Duan, Y., Fu, Q., Ji, W., Cui, H., Jin, D., Lin, Y., and Hu, K.: $O_3$ Sensitivity and Contributions of Different NMHC Sources in $O_3$ Formation at Urban and Suburban Sites in Shanghai, Atmosphere, 11, 295, 10.3390/atmos 11030295, 2020.

Ling, Z., Zhao, J., Fan, S., and Wang, X.: Sources of formaldehyde and their contributions to photochemical $O_3$ formation at an urban site in the Pearl River Delta, southern China, Chemosphere, 168, 1293-1301, 10.1016/j.chemosphere. 2016.11.140, 2017.

Liu, J., Wang, L., Li, M., Liao, Z., Sun, Y., Song, T., Gao, W., Wang, Y., Li, Y., Ji, D., Hu, B., Kerminen, V.-M., Wang, Y., and Kulmala, M.: Quantifying the impact of synoptic circulation patterns on ozone variability in northern China from April to October 2013–2017, Atmos. Chem. Phys., 19, 14477-14492, 10.5194/acp-19-14477-2019, 2019a.

Liu, T., Hu, B., Xu, X., Hong, Y., Zhang, Y., Wu, X., Xu, L., Li, M., Chen, Y., Chen, X., and Chen, J.: Characteristics of $PM_{2.5}$-bound secondary organic aerosol tracers in a coastal city in Southeastern China: Seasonal patterns and pollution identification, Atmos. Environ., 237, 117710, 10.1016/j.atmosenv. 2020.117710, 2020a.

Liu, T., Hu, B., Yang, Y., Li, M., Hong, Y., Xu, X., Xu, L., Chen, N., Chen, Y., Xiao, H., and Chen, J.: Characteristics and source apportionment of $PM_{2.5}$ on an island in Southeast China: Impact of sea-salt and monsoon, Atmos. Res., 235, 104786, 10.1016/j.atmosres.2019.104786, 2020b.

Liu, X., Lyu, X., Wang, Y., Jiang, F., and Guo, H.: Intercomparison of $O_3$ formation and radical chemistry in the past decade at a suburban site in Hong Kong, Atmos. Chem. Phys., 19, 5127-5145, 10.5194/acp-19-5127-2019, 2019b.

Liu, X., Wang, N., Lyu, X., Zeren, Y., Jiang, F., Wang, X., Zou, S., Ling, Z., and Guo, H.: Photochemistry of ozone pollution in autumn in Pearl River Estuary, South China, Sci Total Environ, 754, 141812, 10.1016/j.scitotenv.2020.141812, 2020c.

677 Liu, Z., Wang, Y., Gu, D., Zhao, C., Huey, L., Stickel, R., Liao, J., Shao, M., Zhu, T., Zeng, L., Amoroso, A.,
678 Costabile, F., Chang, C., and Liu, S.: Summertime photochemistry during CARE Beijing-2007:
679 RO<sub>x</s ub> budgets and O< sub>3</sub> formation, Atmos. Chem. Phys., 12, 7737-
680 7752, 10.5194/acp-12-7737-2012, 2012.

681 Lou, S., Holland, F., Rohrer, F., Lu, K., Bohn, B., Brauers, T., Chang, C. C., Fuchs, H., Haeseler, R., Kita, K.,
682 Kondo, Y., Li, X., Shao, M., Zeng, L., Wahner, A., Zhang, Y., Wang, W., and Hofzumahaus, A.: Atmospheric OH
683 reactivities in the Pearl River Delta - China in summer 2006: measurement and model results, Atmos. Chem. Phys.,
684 10, 11243-11260, 10.5194/acp-10-11243-2010, 2010a.

685 Lou, S., Holland, F., Rohrer, F., Lu, K., Bohn, B., Brauers, T., Chang, C.., Fuchs, H., Häseler, R., Kita, K., Kondo,
686 Y., Li, X., Shao, M., Zeng, L., Wahner, A., Zhang, Y., Wang, W., and Hofzumahaus, A.: Atmospheric OH reactivities
687 in the Pearl River Delta – China in summer 2006: measurement and model results, Atmos. Chem. Phys., 10, 11243-
688 11260, 10.5194/acp-10-11243-2010, 2010b.

689 Lu, X., Hong, J., Zhang, L., Copper. O. R., Schultz, M. G., Xu, X., Wang, T., Gao, M., Zhao, Y., Zhang, Y. Severe
690 Surface Ozone Pollution in China: A Global Perspective. Environ. Sci. Technol. Lett., 5, 487-494, 2018.

691 Mao, J., Ren, X., Chen, S., Brune, W. H., Chen, Z., Martinez, M., Harder, H., Lefer, B., Rappenglück, B., Flynn,
692 J., and Leuchner, M.: Atmospheric oxidation capacity in the summer of Houston 2006: Comparison with summer
693 measurements in other metropolitan studies, Atmos. Environ., 44, 4107-4115, 10.1016/j.atmosenv.2009.01.013,
694 2010.

695 Ma, Y., Ma, B., Jiao, H., Zhang, Y., Xin, J., and Yu, Z.: An analysis of the effects of weather and air pollution on
696 tropospheric ozone using a generalized additive model in Western China: Lanzhou, Gansu, Atmos. Environ., 224,
697 117342, 10.1016/j.atmosenv.2020.117342, 2020.

698 Martinez, M.: OH and $HO_2$ concentrations, sources, and loss rates during the Southern Oxidants Study in Nashville,
699 Tennessee, summer 1999, J. Geophys. Res., 108, 10.1029/2003jd003551, 2003.

700 Mazzuca, G. M., Ren, X., Loughner, C.P., Estes, M., Crawford, J. H., Pickering, K. E., Weinheimer, A. J., Dickerson,
701 R. R.: Ozone production and its sensitivity to NOx and VOCs: results from the DISCOVER-AQ field experiment,
702 Houston 2013. Atmos. Chem. Phys. 16, 14463–14474, 2016.

703 Michoud, V., Kukui, A., Camredon, M., Colomb, A., Borbon, A., Miet, K., Aumont, B., Beekmann, M., Durand-
704 Jolibois, R., Perrier, S., Zapf, P., Siour, G., Ait-Helal, W., Locoge, N., Sauvage, S., Afif, C., Gros, V., Furger, M.,
705 Ancellet, G., and Doussin, J. F.: Radical budget analysis in a suburban European site during the MEGAPOLI
706 summer field campaign, Atmos. Chem. Phys., 12, 11951-11974, 10.5194/acp-12-11951-2012, 2012.

707 Nakashima Y , Kato S , Greenberg J , et al.: Total OH reactivity measurements in ambient air in a southern Rocky
708 mountain ponderosa pine forest during BEACHON-SRM08 summer campaign[J]. Atmos. Environ., 85(MAR.), 1-
709 8, 2014.

710 Ren, X., Brune, W. H., Cantrell, C. A., Edwards, G. D., Shirley, T., Metcalf, A. R., and Lesher, R. L.: Hydroxyl and
711 peroxy radical chemistry in a rural area of Central Pennsylvania: Observations and model comparisons, J. Atmos.
712 Chem., 52, 231-257, 10.1007/s10874-005-3651-7, 2005.

713 Rollins, A. W., Browne, E. C., Min, K. E., Pusede, S. E., Wooldridge, P. J., Gentner, D. R., Goldstein, A. H., Liu,
714 S., Day, D. A., Russell, L. M., and Cohen, R. C.: Evidence for NOx Control over Nighttime SOA Formation,
715 Science, 337, 1210–1212, 2012.

716 Saunders, S. M., Jenkin, M. E., Derwent, R. G., and Pilling, M. J.: Protocol for the development of the Master
717 Chemical Mechanism, MCM v3 (Part A): tropospheric degradation of nonaromatic volatile organic compounds,

Atmos. Chem. Phys., 3, 161–180, doi:10.5194/acp-3-161-2003, 2003.

Sheehy, P. M., Volkamer, R., Molina, L. T., and Molina, M. J.: Oxidative capacity of the Mexico City atmosphere – Part 2: A RO<sub>x</sub> radical cycling perspective, Atmos. Chem. Phys., 10, 6993-7008, 10.5194/acp-10-6993-2010, 2010.

Simon, H., Reff, A., Wells, B., Xing, J., and Frank, N.: Ozone trends across the United States over a period of decreasing NOx and VOC emissions, Environ. Sci. Technol., 49, 186-195, 10.1021/es504514z, 2015.

Smith, S. C., Lee, J. D., Bloss, W. J., Johnson, G. P., Ingham, T., and Heard, D. E.: Concentrations of OH and $HO_2$ radicals during NAMBLEX: measurements and steady state analysis, Atmos. Chem. Phys., 6, 1435–1453, doi:10.5194/acp-6-1435-2006, 2006.

Tan, Z., Lu, K., Jiang, M., Su, R., Dong, H., Zeng, L., Xie, S., Tan, Q., and Zhang, Y.: Exploring ozone pollution in Chengdu, southwestern China: A case study from radical chemistry to $O_3$-VOC-NOx sensitivity, Sci Total Environ, 636, 775-786, 10.1016/j.scitotenv.2018.04.286, 2018.

Tan, Z., Lu, K., Jiang, M., Su, R., Wang, H., Lou, S., Fu, Q., Zhai, C., Tan, Q., Yue, D., Chen, D., Wang, Z., Xie, S., Zeng, L., and Zhang, Y.: Daytime atmospheric oxidation capacity in four Chinese megacities during the photochemically polluted season: a case study based on box model simulation, Atmos. Chem. Phys., 19, 3493-3513, 10.5194/acp-19-3493-2019, 2019.

Volkamer, R., Sheehy, P., Molina, L. T., and Molina, M. J.: Oxidative capacity of the Mexico City atmosphere – Part 1: A radical source perspective, Atmos. Chem. Phys., 10, 6969-6991, 10.5194/acp-10-6969-2010, 2010.

Wang, H., Lyu, X., Guo, H., Wang, Y., Zou, S., Ling, Z., Wang, X., Jiang, F., Zeren, Y., Pan, W., Huang, X., and Shen, J.: Ozone pollution around a coastal region of South China Sea: interaction between marine and continental air, Atmos. Chem. Phys., 18, 4277–4295, 10.5194/acp-18-4277-2018, 2018a.

Wang, H., Tan, S., Wang, Y., Jiang, C., Shi, G., Zhang, M., Che, H.: A multisource observation study of the severe prolonged regional haze episode over eastern China in January 2013. Atmos. Environ. 89, 807–815, 2014.

Wang, M., Chen, W., Zhang, L., Qin, W., Zhang, Y., Zhang, X., and Xie, X.: Ozone pollution characteristics and sensitivity analysis using an observation-based model in Nanjing, Yangtze River Delta Region of China, J Environ Sci (China), 93, 13-22, 10.1016/j.jes.2020.02.027, 2020.

Wang, Y., Guo, H., Zou, S., Lyu, X., Ling, Z., Cheng, H., and Zeren, Y.: Surface $O_3$ photochemistry over the South China Sea: Application of a near-explicit chemical mechanism box model, Environ Pollut, 234, 155-166, 10.1016/j.envpol.2017.11.001, 2018b.

Whalley, L. K., Stone, D., Bandy, B., Dunmore, R., Hamilton, J. F., Hopkins, J., Lee, J. D., Lewis, A. C., and Heard, D. E.: Atmospheric OH reactivity in central London: observations, model predictions and estimates of in situ ozone production, Atmos. Chem. Phys., 16, 2109-2122, 10.5194/acp-16-2109-2016, 2016.

Wu, X., Li, M., Chen, J., Wang, H., Xu, L., Hong, Y., Zhao, G., Hu, B., Zhang, Y., Dan, Y., and Yu, S.: The characteristics of air pollution induced by the quasi-stationary front: Formation processes and influencing factors, Sci Total Environ, 707, 136194, 10.1016/j.scitotenv.2019.136194, 2020.

Wu, X., Xu, L., Hong, Y., Chen, J., Qiu, Y., Hu, B., Hong, Z., Zhang, Y., Liu, T., Chen, Y., Bian, Y., Zhao, G., Chen, J., and Li, M.: The air pollution governed by subtropical high in a coastal city in Southeast China: Formation processes and influencing mechanisms, Sci Total Environ, 692, 1135-1145, 10.1016/j.scitotenv.2019.07.341, 2019.

Xue, L. K., Wang, T., Gao, J., Ding, A. J., Zhou, X. H., Blake, D. R., Wang, X. F., Saunders, S. M., Fan, S. J., Zuo, H. C., Zhang, Q. Z., and Wang, W. X.: Ground-level ozone in four Chinese cities: precursors, regional transport

and heterogeneous processes, Atmos. Chem. Phys., 14, 13175-13188, 10.5194/acp-14-13175-2014, 2014.

Xue, L., Gu, R., Wang, T., Wang, X., Saunders, S., Blake, D., Louie, P. K. K., Luk, C. W. Y., Simpson, I., Xu, Z., Wang, Z., Gao, Y., Lee, S., Mellouki, A., and Wang, W.: Oxidative capacity and radical chemistry in the polluted atmosphere of Hong Kong and Pearl River Delta region: analysis of a severe photochemical smog episode, Atmos. Chem. Phys., 16, 9891–9903, 10.5194/acp-16-9891-2016, 2016.

Zeren, Y., Guo, H., Lyu, X., Jiang, F., Wang, Y., Liu, X., Zeng, L., Li, M., and Li, L.: An Ozone "Pool" in South China: Investigations on Atmospheric Dynamics and Photochemical Processes Over the Pearl River Estuary, J. Geophys. Res., 124, 12340-12355, 10.1029/2019jd030833, 2019.

Zhang, K., Duan, Y., Huo, J., Huang, L., Wang, Y., Fu, Q., Wang, Y., and Li, L.: Formation mechanism of HCHO pollution in the suburban Yangtze River Delta region, China: A box model study and policy implementations, Atmos. Environ., 267, 118755, 10.1016/j.atmosenv.2021.118755, 2021a.

Zhang L , Brook J R , Vet R . A revised parameterization for gaseous dry deposition in air-quality models. Atmos. Chem. Phys., 3(2), 2067-2082, 2003.

Zhang, Y., Hong, Z., Chen, J., Xu, L., Hong, Y., Li, M., Hao, H., Chen, Y., Qiu, Y., Wu, X., Li, J.-R., Tong, L., and Xiao, H.: Impact of control measures and typhoon weather on characteristics and formation of $PM_{2.5}$ during the 2016 G20 summit in China, Atmos. Environ., 224, 117312, 10.1016/j.atmosenv.2020.117312, 2020a.

Zhang, Y., Xu, L., Zhuang, M., Zhao, G., Chen, Y., Tong, L., Yang, C., Xiao, H., Chen, J., Wu, X., Hong, Y., Li, M., Bian, Y., and Chen, Y.: Chemical composition and sources of submicron aerosol in a coastal city of China: Results from the 2017 BRICS summit study, Sci Total Environ, 741, 140470, 10.1016/j.scitotenv.2020.140470, 2020b.

Zhang, Y. , Xue, L. , Carter, W. , Pei, C. , and Wang, W.: Development of Ozone Reactivity Scales for Volatile Organic Compounds in a Chinese Megacity, Atmos. Chem. Phys., 10.5194/acp-2021-44, 2021

Zhu, J., Wang, S., Wang, H., Jing, S., Lou, S., Saiz-Lopez, A., and Zhou, B.: Observationally constrained modeling of atmospheric oxidation capacity and photochemical reactivity in Shanghai, China, Atmos. Chem. Phys., 20, 1217-1232, 10.5194/acp-20-1217-2020, 2020.